WILEY

RESEARCH ARTICLE

LiDAR-based characterization of mid-altitude wind conditions for airborne wind energy systems

Markus Sommerfeld[1] | Curran Crawford[1] | Adam Monahan[2] | Ilona Bastigkeit[3]

[1]Institute for Integrated Energy Systems, University of Victoria, Victoria, Canada
[2]School of Earth and Ocean Sciences, University of Victoria, Victoria, Canada
[3]Measurements of environmental conditions, Fraunhofer Institute for Wind Energy Systems IWES, Bremerhaven, Germany

Correspondence
Markus Sommerfeld, PO Box 1700 STN CSC, Victoria BC V8W 2Y2.
Email: msommerf@uvic.ca

Summary

Engineers and researchers working on the development of airborne wind energy systems (AWES) still rely on oversimplified wind speed approximations and coarsely sampled reanalysis data because of a lack of high-resolution wind data at altitudes above 200 m. Ten-minute average wind speed LiDAR measurements up to an altitude of 1100 m and data from nearby weather stations were investigated with regard to wind energy generation and impact on LiDAR measurements. Data were gathered by a long-range pulsed Doppler LiDAR device installed on flat terrain. Because of the low overall carrier-to-noise ratio, a custom-filtering technique was applied. Our analyses show that diurnal variation and atmospheric stability significantly affect wind conditions aloft which cause a wide range of wind speeds and a multimodal probability distribution that cannot be represented by a simple Weibull distribution fit. A better representation of the actual wind conditions can be achieved by fitting Weibull distributions separately to stable and unstable conditions. Splitting and clustering the data by simulated surface heat flux reveals substate stratification responsible for the multimodality. We classify different wind conditions based on these substates, which result in different wind energy potential. We assess optimal traction power and optimal operating altitudes statistically as well as for specific days based on a simplified AWES model. Using measured wind speed standard deviation, we estimate average turbulence intensity and show its variation with altitude and time. Selected short-term data sets illustrate temporal changes in wind conditions and atmospheric stratification with a high temporal and vertical resolution.

KEYWORDS

airborne wind energy, airborne wind energy power estimate, lower tropospheric wind characterization, mid-altitude wind characterization, mid-altitude wind speed probability distribution, onshore LiDAR measurements

1 | INTRODUCTION

The objective of this study is to characterize prevailing wind conditions for load estimation and system optimization of airborne wind energy systems (AWES) at mid-altitudes, here defined as heights above 100 m and below 1500 m. AWES are a novel renewable energy source that harvest stronger lower tropospheric winds at altitudes, which are unreachable by current wind turbines, at potentially much reduced capital cost.[1,2] Some proponents advocate the development of high-altitude devices that are supposed to operate at thousands of meters (altitudes at which no current measurement devices can practically measure with sufficiently high sampling frequency). For practical and economical reasons, we focus on resource assessment within the lower part of the atmosphere, an altitude range spanned by the highly variable boundary layer (with depths as little as tens of meters at night and a few kilometers during the day). Unlike conventional wind energy, which has converged to a single design with three blades and a conical tower, several different AWES designs are under investigation by many companies and research institutes.[3] Various concepts from ring-shaped aerostats, from rigid wings to soft kites with different sizes, rated power and altitude ranges compete for entry into the marketplace. Since this technology is still in an early stage, none are currently commercially available. If the trend toward taller towers and longer turbine blades continues, conventional wind turbines will also operate at mid-altitudes in the future and
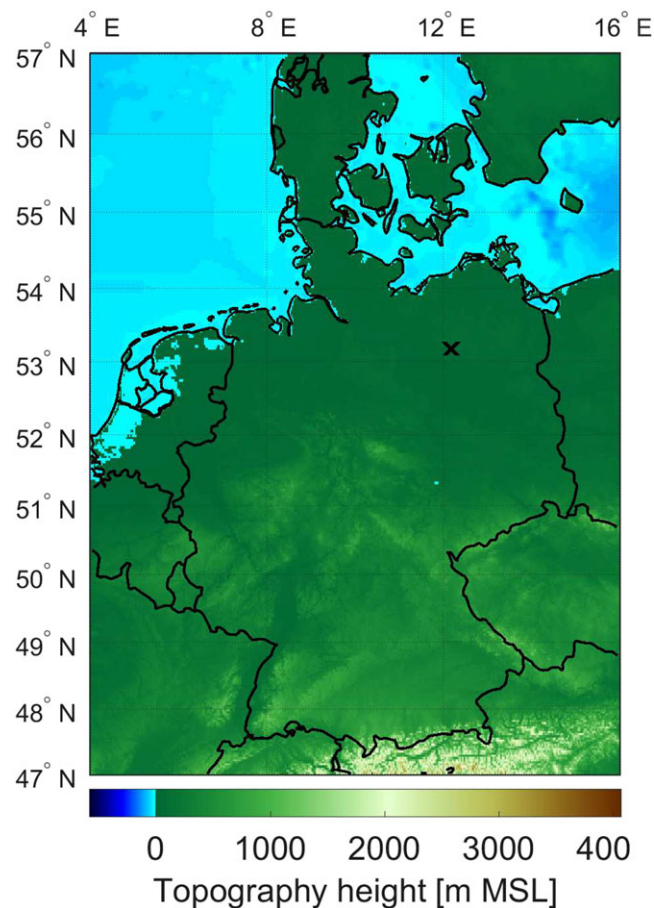
FIGURE 1 Topographic map in northern Germany close to Pritzwalk with the measurement site marked by a black *X* [Colour figure can be viewed at wileyonlinelibrary.com]

experience significantly different wind conditions than close to the surface. Developers and operators therefore require accurate information to estimate the power production and mechanical loads.

We investigate the wind resource up to 1100 m over generally flat terrain at Pritzwalk in northern Germany (see map in Figure 1). The measurement campaign lasted 6 months between September 2015 and February 2016 with the objective of estimating the wind energy potential at altitudes higher than usually observed for this application. In contrast to the low level winds in the first few hundred meters of the atmosphere, mid-altitude winds from a few hundred meters to about 1500 m have not often been investigated. Recent advancements in wind light detection and ranging (LiDAR) technology enabled high temporal and vertical resolution measurements in higher altitudes. This enables a detailed analysis of specific wind conditions as well as statistical evaluation necessary for the development of AWES. Furthermore, these data are able to extend and supplement established knowledge of wind speed profiles and wind speed probability distributions under different atmospheric stability conditions as well as diurnal variations at higher altitude than tower measurements allow. The common way to gather wind and weather data at these altitudes are sparsely deployed weather balloons (radiosondes), which measure data while quickly ascending through the atmospheric boundary layer (ABL).[4] This measurement technique does not offer continuous data acquisition and has an inherently low temporal and vertical resolution. The low temporal resolution of radiosondes leads to considerable undersampling and a loss of higher frequency information. Nonetheless, this measurement technique offers an estimate of the global wind resource in higher altitudes.[5] Engineers and researchers had to rely on coarsely resolved reanalysis data sets or oversimplified approximations such as the logarithmic wind profile to assess the potential of AWES.[6-8] While reanalysis data provide good global and long-term information, it cannot capture local and short-term variations. Remote sensing devices such as long-range pulsed LiDAR enable the measurement of wind speeds up to several thousand meters away from the point of deployment. These devices measure the spectral shift between the emitted light pulse and the returning light backscattered of aerosols transported with the wind.[9] The aerosol load of the air therefore limits the data availability of this measurement technique. The aerosol load decreases with altitude and drops to levels so low that LiDAR devices are not able to measure winds at these altitudes, as the primary aerosol source is the Earth's surface.[10]

Surface heat flux (SHF) or temperature information is required to characterize different stability condition within the ABL, both of which were not directly measured. Mesoscale numerical weather prediction models such as the Weather Research and Forecasting (WRF) model provide detailed data sets at higher resolution compared with reanalysis data. We make use of the sign of the WRF simulated SHF for statistical analyses and assume the sign of the SHF to be better simulated than sign and magnitude.[11,12] However, temporal difference of times associated with positive and negative SHF between model and measurement will lead to occasional mismatch of transition times[13] as well as random errors. We

believe that these errors are statistically insignificant for the overall evaluation but are aware of the resulting inaccuracy. A detailed discussion of the WRF simulations will be presented in a later publication.

We estimate power production per unit lifting area based on a simplified traction power model by Schmehl et al.[14] This quasi steady state model includes losses due to misalignment of wind direction and AWES position but neglects gravity, tether drag, and detailed flight maneuvering. We can therefore assess the upper limit on traction power and optimal operating altitude for the whole measurement period, different stratification conditions as well as specific wind speed profiles.

Section 2 defines the necessary conventions. Section 3 describes the wind LiDAR measurement campaign, the filtering technique, and the impact of data availability. Section 4 consists of a detailed statistical analysis of wind speed, direction, turbulence intensity (TI) as well average diurnal variation and exemplary wind conditions. Section 5 estimates the traction power and optimal operating altitude. Finally, the results are summarized and an outlook for future work is given in section 6.

2 | DEFINITIONS

Most of the available LiDAR data we consider are within the ABL, the actively turbulent region of the troposphere, which is directly influenced by surface forcing such as heat transfer, evaporation and friction.[15] Its height varies from as low as a few tens to thousands of meters above ground, depending on location and time. The lowest part of the ABL, the atmospheric surface layer (ASL) accounts for roughly 10% of the ABL and is greatly affected by the surface and diurnal changes. The region of the troposphere above the ABL is referred to as the free atmosphere, which is almost unaffected by diurnal variation because of very weak direct interaction with the surface.[15] Processes within the ABL depend on stratification that is, among other processes, influenced by surface absorption of solar irradiation, energy fluxes, and horizontal advection. A distinction between a statically *stable*, *neutral*, and *unstable* stratification is made based on temperature (and to a lesser extent water content) profiles. Unstable stratification is characterized by strong vertical mixing and high TI because of the additional production of turbulent kinetic energy by buoyancy. In a stable stratification, vertical displacement of air parcels requires work to be done against the stratification.

This article investigates 10-minute average horizontal wind speeds U directions. Wind direction is defined according to meteorological convention. North is defined as 0° and a positive directional change refers to a clockwise rotation, so 90° refers to east, 180° south, and 270° west. We normally expect a clockwise rotation with height for "ideal" boundary layer winds in the northern hemisphere,[16] caused by the adjustment of ABL velocity fields to geostrophic conditions. This directional change is referred to as the "Ekman spiral."[15] However, horizontal temperature gradient "thermal winds" can significantly influence the shape of the wind shear profile.

The wind profile over homogeneous, flat terrain is often estimated by a logarithmic wind profile with a correction to account for stratification:[17,18]

$$U = \frac{u_*}{\kappa} \left[\ln \left(\frac{z}{z_0} \right) - \Psi_m(z, z_0, \mathcal{L}) \right]. \tag{1}$$

This approximation, which does not apply to mid-altitude and high-altitude winds above the ASL, describes the horizontal wind speed U at altitude z as a function of friction velocity u_*, aerodynamic roughness length z_0, and Kármán constant κ. The stability function Ψ_m accounts for the atmospheric stability conditions (stable, unstable, neutral), which is a function of the Obukhov length $\mathcal{L}$, altitude z, and surface roughness z_0.[15]

3 | MEASUREMENT CAMPAIGN

The data were collected between September 1, 2015, and February 29, 2016 at the "Pritzwalk Sommersberg" airport (Coordinates: Lat: 53° 10' 47.00"N, Lon: 12° 11' 20.98"E) in northeast Germany (marked by a black X in Figure 1) using a single beam pulsed wind LiDAR from SgurrEnergy.[51] The area around the airport is mostly flat agricultural land with a village to the south, a small forest in the southeast, and a wind park about 3.5 km to the west.

After an extended power outage between December 7 and December 11, data quality in terms of carrier-to-noise ratio (CNR) decreased. The reason for this could not be identified. A custom filtering technique was applied to increase data availability. It is possible that incorrect settings, a return to default settings or issues with the laser were responsible for the reduced data quality.

3.1 | Wind LiDAR

Doppler LiDAR devices measure the frequency shift of the backscattered laser beam caused by the movement of aerosols carried by the wind. This shift is proportional to the line-of-sight (LOS) particle velocity. Multiple measurements can therefore be used to calculate the wind velocity from which the horizontal wind speed can be inferred. The here used Galion 4000 from SgurrEnergy is able to measure wind speed and direction up to 4000 m away from the device and offers various scan methods such as "ArcScan" and doppler beam swinging (DBS).[19] DBS scans usually take 4 and/or 5 measurements at constant elevation angle and varying azimuth angle. Assuming a horizontally homogeneous wind field, LOS measurements at constant height can be fitted to a sine function from which the wind speed and direction within the scanned volume are calculated. With the LiDAR device located at an air field on flat terrain, it is a reasonable approximation that the environmental conditions are

similar within the LiDAR's sampling area. As the elevation angle is kept constant, in our case 62° (28° to horizon), during DBS scans, the averaging area increases with altitude. At an altitude of 1100 m, the radius of the disc defined by the four azimuth positions with 90° increments is about 585 m. Reorientation of the laser beam toward the next azimuth position led to measurement intervals between 3 to 5 seconds. From these LOS measurements, we determined the 10-minute average wind speeds at 40 range gates between 66 and 1099 m above ground in 26.5-m increments. The focal length of the laser beam was set to 800 m.

The Galion4000 LiDAR was verified against a WindCubeV2 (according to IEC 61400-12-1,[20]) at the Fraunhofer Institute for Wind Energy Systems (IWES) Bremerhaven during a validation period of 1 week before deployment. Wind speeds up to an altitude of 260 m were compared, and a linear regression between the measurements showed a 99% accordance between both devices. Since data quality was sufficiently high, we refrained from a simultaneous deployment of the WindCubeV2.

3.2 | Data processing

Wind LiDAR data quality is impacted by various effects, some of which will be examined in this chapter. Generally, data quality highly depends on the backscatter from aerosols in the air. Aerosol content in higher altitudes is dictated by mixing and settling as most of the particles originate from the surface. This leads to an overall decrease of backscatter with altitude. Cloud cover increases the backscatter within the lower part of the cloud while it prevents laser beams from penetrating to higher altitudes. Data quality, according to which LiDAR measurements are further filtered, is generally described by the CNR:

$$CNR_{dB} = 10 \log_{10}\left(\frac{C}{N}\right). \tag{2}$$

CNR is defined by the ratio between the power contained in the signal C to the power contained in the noise N over the full detector bandwidth. Multiple quality criteria were applied to the raw data. First, a sufficient number of LOS wind speed scans must be gathered to calculate 10-minute average wind speed. Based on these individual measurements, average 10-minute mean CNR values are calculated for further filtering.[21] Several studies showed that the selection of a CNR threshold impacts the mean wind speed estimation.[22,23]

During the measurement campaign the average CNR remained almost constant up to the focal length of 800 m. The CNR trend does not show the distinct peak at the set focal length, which is reported in other publications.[16] A long focal length seems to prevent the steep decrease of CNR above the set focal length.[9] The overall CNR decreased by approximately 5 dB over 1000 m.

While the manufacturer proposed a fixed CNR threshold of -20 dB,[24] other publications suggest the use of a threshold of -22 dB.[25] Figure 2 illustrates the data availability as a function of altitude and CNR threshold.

Applying a -20dB CNR filter leads to an availability of about 23% at 1000 m, which is relatively high compared with other publications.[16] However, applying this filter leads to a low data availability of only 77.5% at 66 m. To counteract the low availability at low altitudes, we apply a CNR threshold of $CNR_{dB} > -25$ dB combined with additional filters to reduce the noise and correct for obvious mismeasurements. The following thresholds were applied to all measurements:
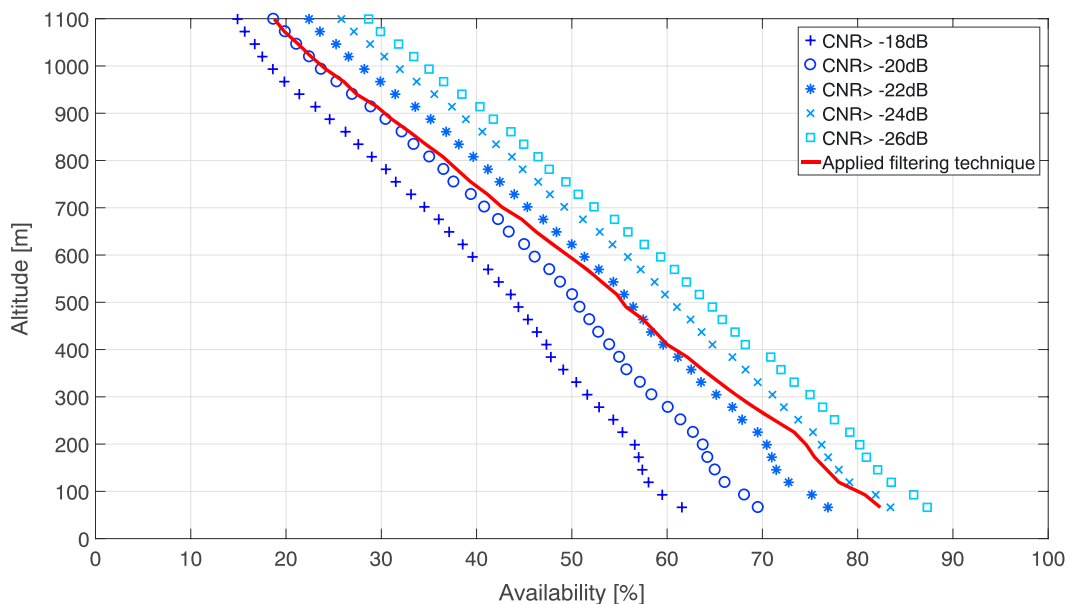

FIGURE 2 Wind light detection and ranging availability as a function of 10-minute mean (CNR) carrier-to-noise ratio filters (blue markers) and altitude. The red line indicates availability after applying the self-defined filter [Colour figure can be viewed at wileyonlinelibrary.com]
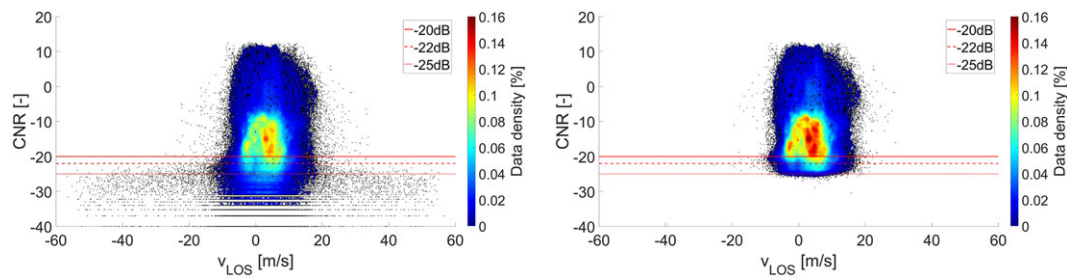
FIGURE 3 Comparison of unfiltered (left) and filtered (right) light detection and ranging carrier-to-noise ratio (CNR) over light of sight wind speed for the whole measurement campaign. Red lines indicate commonly applied constant CNR thresholds [Colour figure can be viewed at wileyonlinelibrary.com]

- $CNR_{dB} > -25$ dB,
- $U > 0 m/s$,
- $U < 45 m/s$,
- $U < 2.5 \cdot U(z = 150 m)$,
- min scan count $> 40\%$.

The "scan count" criterion defines the minimum amount of backscatter measurements that are necessary to calculate the 10-minute average wind speed. As a result, the overall data availability of 10-minute averages increased while availability with altitude decreases from about 81% at 100 m and to about 24% at 1000 m.

Investigation of the 10-minute average radial wind speed U_{LOS} and the CNR at all altitudes shows a data cluster between $-10 m/s < U_{LOS} < 20 m/s$ with CNR values above -30 dB (see Figure 3). The reason for the shift of the data center toward positive LOS velocities could not be definitely determined. It could indicate an inhomogeneous wind field. However, the analyzed horizontal wind speed is unaffected by this shift.[26] Three constant threshold filters are denoted by the red lines for reference. Data points below the -22-dB threshold show a significant, unrealistic wind velocity spread of up to ± 60 m/s. 31.1% of the unfiltered measurements are below the -20-dB threshold. The right figure shows the data distribution after applying the self-defined filtering criteria. There seems to be no indication that data within the high data density region but below the CNR threshold is invalid.[27] Based on this assumption, the applied filtering technique can be considered conservative as it cuts off CNR values below -25 dB, which are within the LOS wind velocity range of approximately ± 15 m/s. As a result of the application of the self-defined filters, the overall data availability increased by approximately 15% in comparison to the fixed -20-dB threshold filter while unrealistic values were filtered out.

3.2.1 | Weather impact on data quality and availability

Weather phenomena such as rain, fog, and cloud coverage impact the overall LiDAR data availability, because of the proportionality of backscatter and aerosol content in the air. Weather stations close the LiDAR location gathered precipitation (Perleberg: about 30 km from the LiDAR) and cloud coverage data (Neuruppin: about 58 km from the LiDAR). Figure 4 shows the daily average cloud cover and cumulative daily rain fall close to the measurement location throughout the entire campaign.

Extensive cloud coverage or fog increases the availability close to the LiDAR because of the high amount of backscattering particles or water droplets. This is the reason for a higher backscatter intensity within clouds than during clear sky conditions.[16,29] However, this also reduces the distance that laser beams penetrate into the cloud or fog, often leading to data loss aloft. Determining a direct correlation between cloud cover and data availability is difficult and would require additional measurements such as aerosol concentration gathered by a ceilometer; cloud cover does not give information on cloud height. However, the overall high cloud coverage throughout the entire campaign is one of the reasons for low data availability aloft.

Figure 5 shows an example where cloud coverage prevents high-altitude measurements. Here, measured CNR is compared to hourly cloud coverage and precipitation for 4 days in September 2015 to correlate weather data with LiDAR data quality. The high CNR between September 11 and September 13 correlates well with the presence of clouds above which no data could be gathered (yellow: high CNR, blue:low CNR, white: no data). The lack of high altitude data on September 14 could be caused by rain as the weather station in Perleberg shows a high precipitation of up to 6 mm/m^2. However, no definite correlation between altitude-dependent CNR and cloud coverage can be proven without additional cloud height measurements.

Another factor to consider when investigating the LiDAR data availability aloft is that the density of aerosols not only decreases with altitude, but also drops to a level that is too low to detect with current LiDAR or ceilometer technology.[30] The altitude at which this drop occurs is referred to as mixing layer height, which is defined as the height up to which thermally induced vertical dispersion of air pollutants takes place.[31] Therefore, the height of the mixing layer is highly dependent on stratification and time as it will lose aerosol particles because of settling. The backscatter intensity can give an estimate of the mixing layer aerosol load and height.[32,33] In the example below, it is likely that the height of the cloud layer (yellow area) between September 12 and 13 also gives a good estimate of the ABLH.[25] The WRF model mostly supports this assumption as it calculates an ABLH (black line in Figure 5) below 200 m between 18:00 UTC on September 12 and 10:00 UTC on September 13.
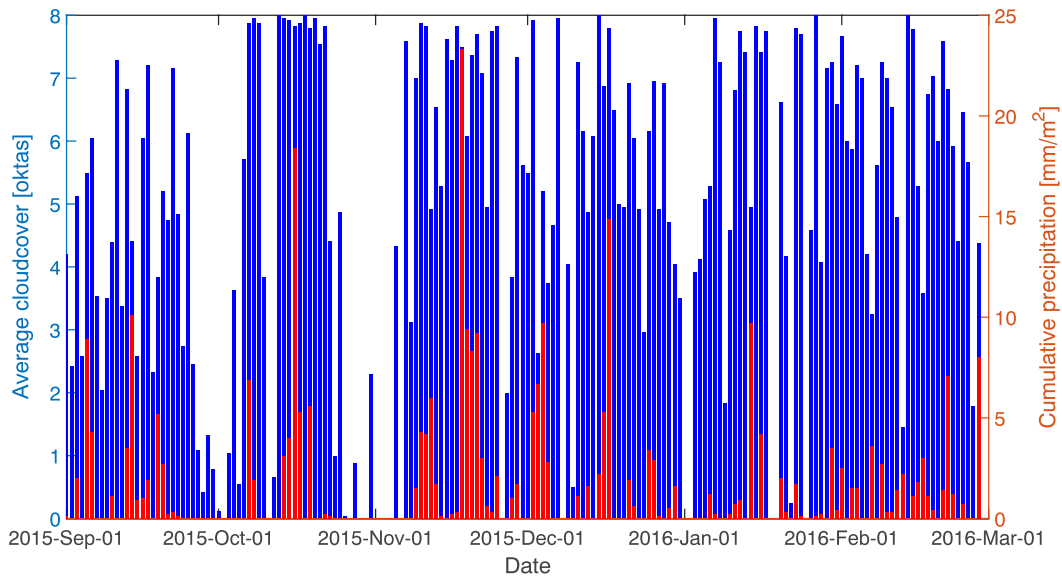
FIGURE 4 Accumulated precipitation (weather station Perleberg about 30 km from light detection and ranging) and daily average cloud cover (weather station Neuruppin about 58 km from LiDAR), data source provided by Deutscher Wetterdienst—Germany's National Meteorological Service[28] [Colour figure can be viewed at wileyonlinelibrary.com]
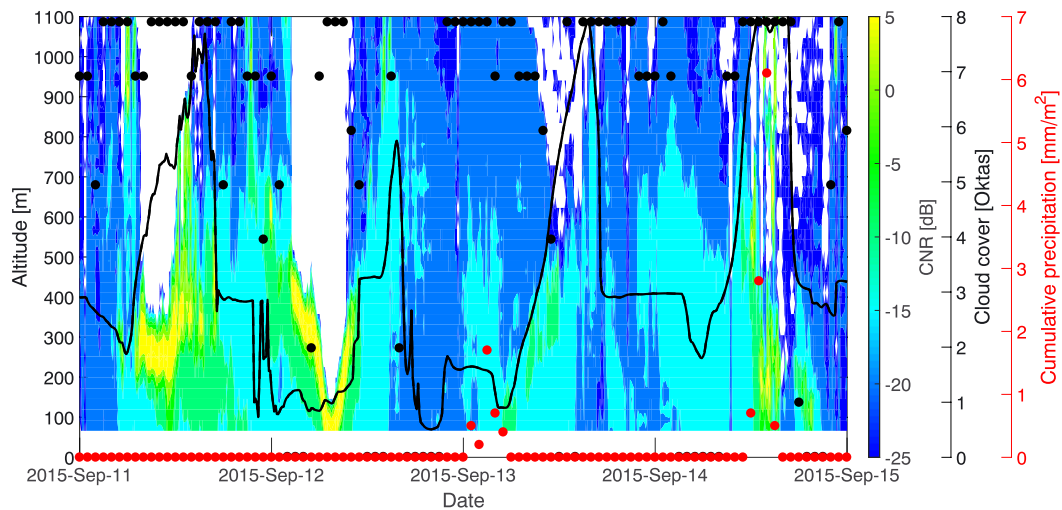

FIGURE 5 Contour of light detection and ranging CNR over altitude from September 11 to September 15, 2015. The black line shows the Weather Research and Forecasting-calculated atmospheric boundary layer height. Black dots denote hourly average cloud coverage at the Neuruppin weather station (about 58 km away from light detection and ranging). Red dots denote hourly average precipitation at weather station Perleberg (about 30 km from light detection and ranging) [Colour figure can be viewed at wileyonlinelibrary.com]

3.2.2 | Impact of diurnal variation and surface heat flux on data quality

Atmospheric aerosols mostly derive from the surface and therefore depend on vertical mixing to be transported aloft. This vertical mixing within the ABL is dictated by the diurnal cycle of the vertical SHF. An investigation of altitude dependent, hourly average diurnal variation of LiDAR availability (see Figure 6) shows substantial decrease with altitude and distinct diurnal variation. After sunrise, enhanced vertical mixing and surface winds lead to an upward transport of particles, increasing the availability aloft and decreasing it near the surface. The reduction in low-level availability seems to occur shortly after sun rise, while the increase at higher altitudes occurs slightly later. This delay results from the time required for buoyancy induced upward transport of particles to lead to their accumulation aloft. Altitude dependent layers of almost constant availability develop. Such layers above approximately equal to 500 m remain at an almost constant height throughout the day but shift upwards during daytime. Availability peaks are seemingly simultaneous between 16:00 and 17:00 UTC at these altitudes. In contrast, average availability remains almost constant at about 250 m. As a result, any analysis of the total measurement data set will be slightly biased by diurnal variation in LiDAR data availability.

To circumvent this issue, the data set can either be segmented by time of day or atmospheric stratification. Positive SHF is associated with unstable stratification where buoyancy-induced vertical mixing leads to relatively lower wind shear aloft. Negative SHF and stable stratification
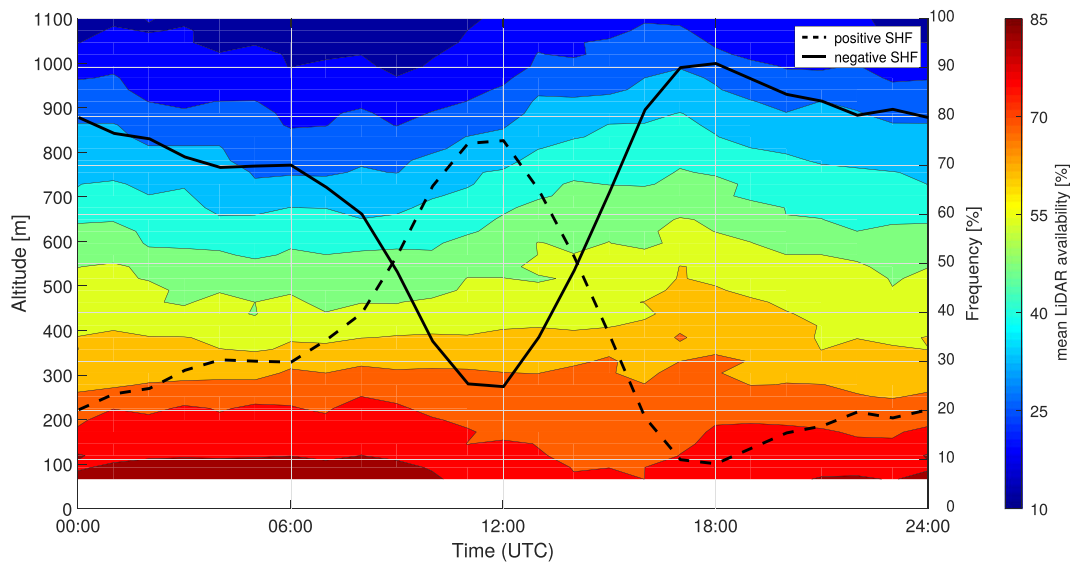
FIGURE 6 Hourly average diurnal variation of light detection and ranging (LiDAR) availability over altitude after filtering and Weather Research and Forecasting-calculated positive (dashed line) and negative (solid line) surface heat flux sign [Colour figure can be viewed at wileyonlinelibrary.com]

inhibit mixing and lead to higher wind shear.[15] Positive heat flux is most often associated with daytime, and negative heat flux is usually associated with nighttime. However, the impact of SHF is reduced by high wind speeds. Data are partitioned by WRF[34] calculated SHF sign, since the LiDAR device itself was not equipped to gather such information. The WRF model consisted of three nested domains driven by ERA-Interim[35] reanalysis data using the Mellor Yamada Nakanishi Niino (MYNN) 2.5 planetary boundary layer scheme.[36] The inner domain had a grid spacing of 3 x 3 km and a temporal output resolution of 10 minutes. A detailed description will be given in a future publication. Figure 6 shows the diurnal variation of hourly average WRF-modeled SHF sign. Overall, negative SHF is almost twice as likely to occur during the entire measurement campaign than positive heat flux (70 % vs 30%).

Comparing availability associated with different stratification reveals that times of positive SHF show an almost 5 % higher than average LiDAR availability, while availability during negative SHF is about 2.5 % lower than average at altitudes below 300 m. Between 600 and 900 m, the availability of both positive and negative heat flux matches the average availability. Above 900 m, time periods experiencing negative SHF show a slightly increased availability, and times of positive SHF have a lower availability than average. Time-delayed vertical buoyant aerosol transportation, which affects lower altitudes quicker than higher altitudes, probably leads to the inversion at high altitudes.

4 | WIND MEASUREMENT ANALYSIS

We present a statistical analysis of the entire wind LiDAR data set as well as some detailed findings for a few selected days in September 2015. It is important to keep the reduced data availability in mind when comparing the statistics for different altitudes. Diurnal variability causes altitude dependent conditional sampling of wind speeds, which leads to differences between measured and real wind conditions as data can only be gathered when the meteorological conditions allow it. Furthermore, the measurement campaign only lasted 6 months covering autumn and winter (September to February). Annual wind statistics will differ as winds are generally stronger during this season.[22]

4.1 | Average wind conditions and Weibull distribution fit

Figure 7 visualizes the wind speed probability distribution (left column) and quantifies the difference between it (right column) and the standard Weibull distribution fit (center column—see Equation 3) to determine whether the Weibull fit is an adequate tool to describe mid-altitude winds. The Weibull fit is defined by:

$$f_{Weibull}(u) = \frac{k}{A}\left(\frac{u}{A}\right)^{k-1} e^{-\left(\frac{u}{A}\right)^k},$$

(3)

where A is the Weibull scale parameter in m/s and k is the unitless Weibull shape parameter.[37] All data were binned into 0.5-m/s intervals. By conditioning the total data set (bottom row) by the SHF sign (positive SHF: top row; negative SHF: center row), two distinct populations become apparent. This segmentation is solely based on the mathematical sign of the WRF modeled SHF.

The total wind speed probability distribution (g) has bimodal characteristics above approximately 200 m. This bimodality is isolated by conditioning the data on SHF sign, resulting in two distinct distributions of wind speeds at times of positive (a) and negative heat flux (d). Times of
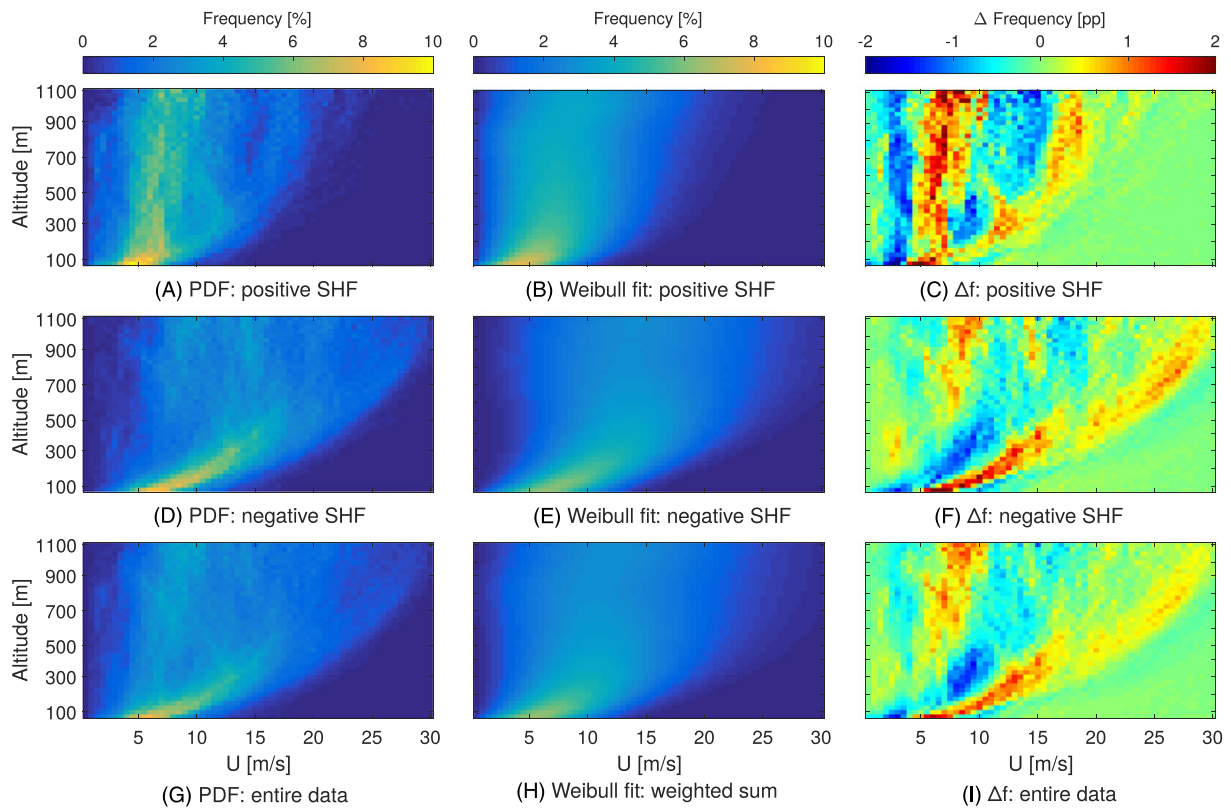
FIGURE 7 Comparison of wind speed frequency based on light detection and ranging measurements (left column), corresponding Weibull fit (center column) and the difference between both ($\Delta f = f_{LiDAR}(U) - f_{Weibull}(U)$) in percentage points (pp) (right column) over altitude binned into 0.5-m/s intervals. Top row corresponds to times of positive SHF and center row to times of negative SHF, and bottom row shows total data set. The Weibull fit in the bottom row is the weighted sum of positive and negative Weibull fits, weighted by the respective overall occurrence [Colour figure can be viewed at wileyonlinelibrary.com]

TABLE 1 Frequency of atmospheric stratification based on the sign of Weather Research and Forecasting-calculated surface heat flux and K-mean clustering using all 40 LiDAR range gates

| | Positive Heat flux | | Negative Heat Flux | |
	Unstable	Shear driven	Weakly stable	Very stable
Heat flux	29.07 %		70.93 %	
K-means cluster	20.32 %	8.75 %	36.30 %	34.64 %

positive SHF are associated with higher thermal mixing and an unstably stratified boundary layer, resulting in a high frequency of lower, almost constant wind speeds up to high altitudes.[38] For our data set, positive SHF is associated with lower geostrophic winds as the wind speeds aloft tend to be lower compared to times of negative SHF. Furthermore, the probability distribution still shows the existence of a second state with higher wind speeds. Possible reasons for the existence of this second state are misclassification of observed wind profiles by simulated SHF, transient evolution of the profiles, or strong large-scale pressure gradient forces, which can reduce the influence of stratification on wind profiles. As a result, the Weibull distribution, with almost no broadening above 200 m and a lower median wind speed throughout all measured heights, underestimates the frequency of both substates. Based on measurements, the likelihood of wind speeds between 5 and 7 m/s is higher than the Weibull fit suggests.

Times of negative SHF are associated with a stably stratified boundary layer and buoyant consumption of turbulent kinetic energy, which results in higher wind shear and higher wind speeds. Measurements during negative SHF (d) show an increased probability of high wind speeds and a strong wind shear in the lower part of the atmosphere, distinctly different from wind conditions under positive SHF. The distribution broadens aloft leading to an almost even distribution at high altitudes, with very low chance of low wind speeds, which are most probable during positive SHF. Looking at the difference between measured distribution and the Weibull fit, both high and low wind speeds aloft as well as the very narrow band of wind speeds below are not well represented.

The bottom row summarizes the total wind speed probability distribution and weighted sum of the two Weibull fits for times of positive and negative SHF. The weighting factor is the likelihood of positive and negative heat flux summarized in Table 1 (first row). This bimodal distribution
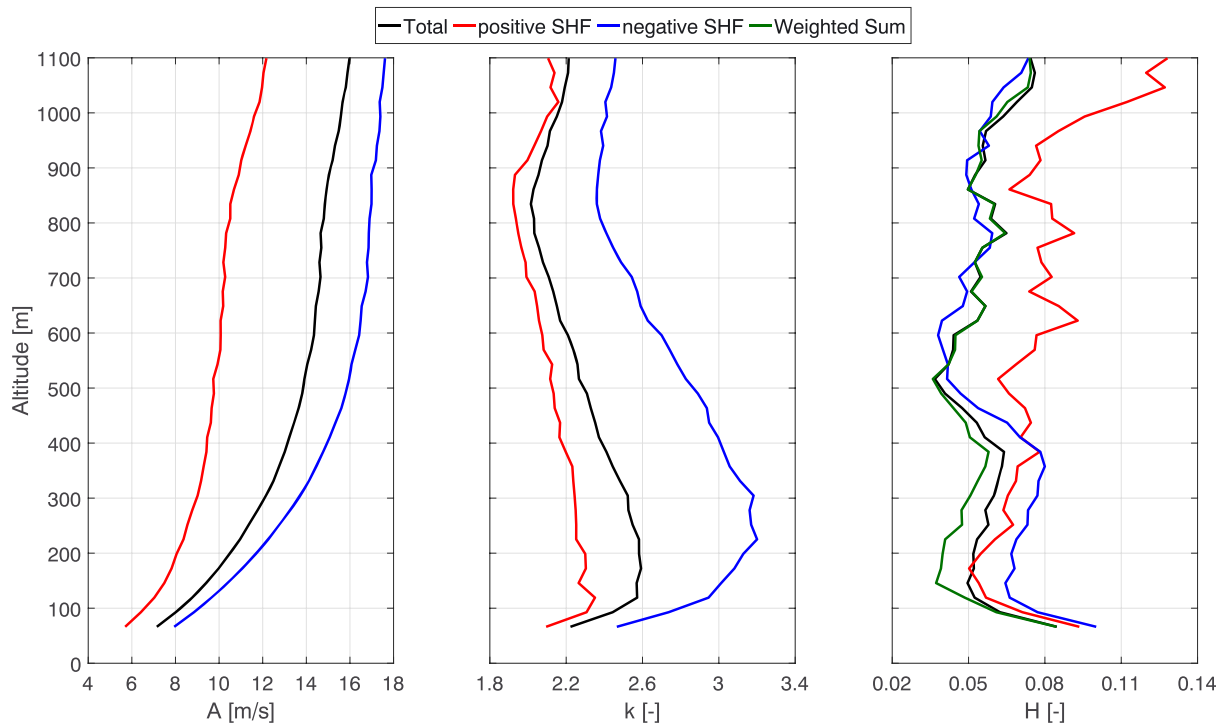
FIGURE 8 Weibull scale *A* and shape parameter *k* over altitude calculated based on the entire 6 month measurement campaign. Results based on the whole data set are shown in black, positive surface heat flux (SHF) in red, and negative SHF in blue. The respective Hellinger distance (*H*) between the measured probability distribution and the Weibull fit is shown on the right. Additionally, the Hellinger distance between the total probability distribution and the frequency of occurrence (see Table 1) of the weighted sum of both SHF Weibull fits is shown in green [Colour figure can be viewed at wileyonlinelibrary.com]

still can not represent the high frequency of very low and high wind speeds but presents an improvement on fitting the complete data set with a single Weibull function.

The total Weibull scale *A* and shape parameter *k* shown in Figure 8 follow expected trends for the winter season over flat land. The shape parameter peaks below 100 to 250 m and the scale parameter follows a logarithmic trend.[39,40] The SHF classified data sets show distinctly different trends, with negative SHF being associated with high values of *A* and a peak in *k* between 200 and 300 m, which is consistent with Monahan et al.[41] Positive heat flux on the other hand leads to a relatively slow increase of *A* as well as lower *k* values that decline almost linearly with altitude. The Hellinger distance (*H*) between the probability distribution of the measured data set and the corresponding Weibull fit quantifies the goodness of fit. The weighted sum (green) of both positive (red) and negative SHF (blue) Weibull fits represents the multimodal nature of the wind speed measurements up to 500 m better than the simple Weibull fit (black), indicated by a lower *H*. High *H* for times of positive and negative SHF is likely caused by the existence of additional states, suggested by Figure 7.

To further distinguish the substates, we use *K-means clustering* on both SHF-partitioned data sets, to identify two additional clusters within each SHF-sign condition. These results are highly affected by data availability as time steps with any missing data where discarded. Therefore, only measurements where all 40 range gate measurements were available were used to calculated the probability distribution and cluster centroids (white square) shown in Figure 9. Clustering the data based on lower range gates lead to lower overall wind speeds, indicating an availability bias toward higher winds speeds caused by increased vertical mixing and horizontal transportation of aerosols. However, clustered based on lower altitudes maintained similar probability distributions showing the same substates. The respective frequency of each substate is summarized in Table 1. The first cluster of positive SHF (a) which occurs around 20.3% of the time displays very low wind speed and shear, which is typical for an unstable boundary layer with weak large-scale pressure gradients. The second cluster of positive SHF (b) appears to be a shear driven and has a frequency of only about 8.7%. The first cluster of negative SHF (c) represents weakly stable boundary layer with relatively high wind speeds and strong wind shear up to high altitudes. The second cluster of negative SHF (d)shows relatively low wind speeds and well-developed near-surface jets. Characteristic shear profiles of different stability conditions are consistent with Monahan et al[42] and extend to even higher altitudes. Both stable states (bottom) have an almost equal frequency at 36.3 % and 34.6 %. The nonconverging wind speeds aloft are associated with different large-scale conditions driving these phenomena.

These results show that AWES and very large conventional wind turbines operating at mid-altitudes will have to function across a wide range of wind conditions. AWES need to be able to withstand more probable extreme loads caused by high wind speeds, while still being able to navigate through calm periods. Furthermore, as wind conditions vary so significantly, optimal operating altitude and power highly depend on atmospheric stratification as will be shown in section 5. This highlights the need for long-term, high-resolution measurements to determine the ideal operating altitude as well as estimating the energy yield at a given location.
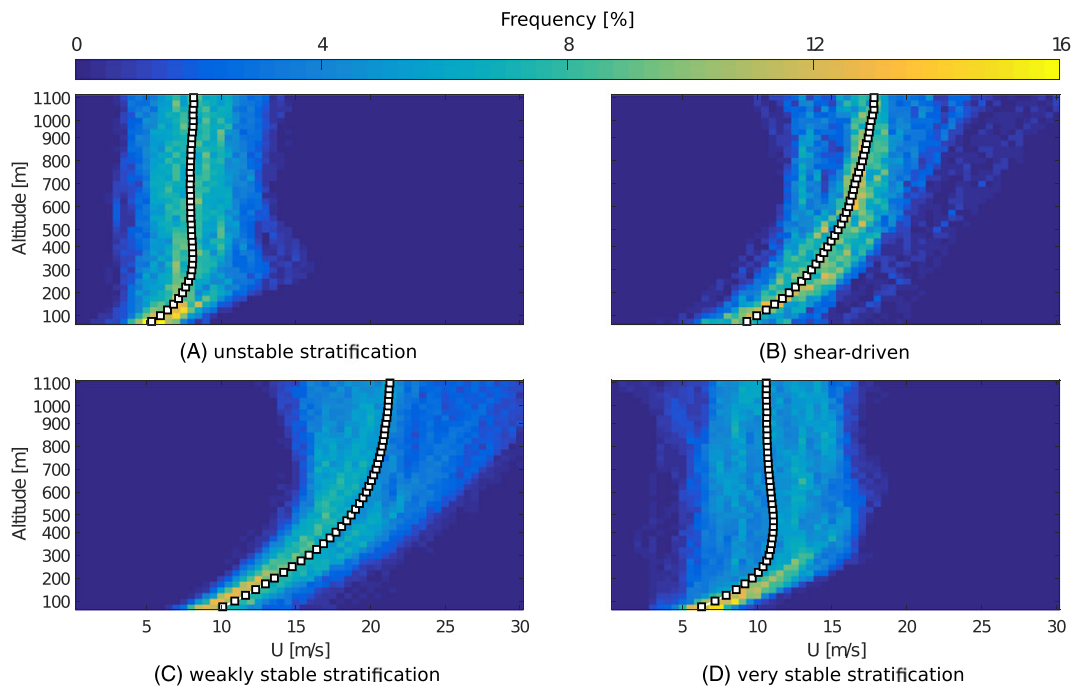
FIGURE 9 K-means clustered probability distribution (each altitude adds up to 100%) and centroids (white squares) of wind speeds preallocated by Weather Research and Forecasting-calculated surface heat flux. Table 1 summarizes the frequency of occurrence of each cluster. Top left: unstable stratification, top right: shear driven, bottom left: weakly stable stratification, bottom right: very stable stratification
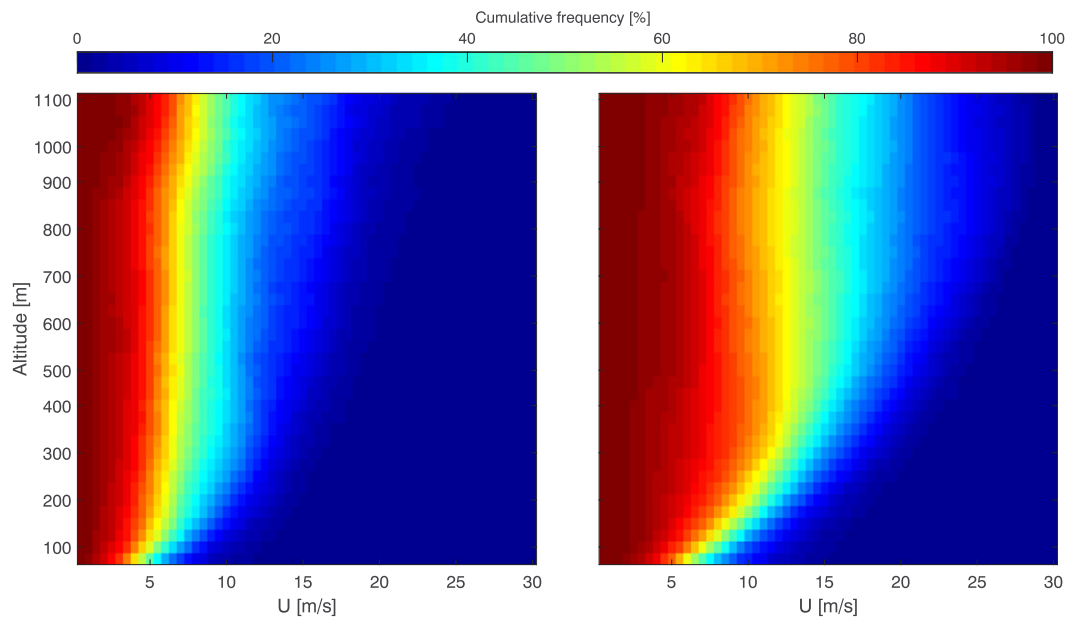

FIGURE 10 Inverse cumulative light detection and ranging wind speed probability distribution of the whole measurement campaign over altitude split by surface heat flux calculated in Weather Research and Forecasting. The left side represents times of positive surface heat flux (unstable stratification), the right side represents times of negative surface heat flux (stable stratification) [Colour figure can be viewed at wileyonlinelibrary.com]

4.2 | Inverse cumulative wind speed probability distribution

The inverse cumulative density function in Figure 10 highlights the probability a certain wind speed is exceeded at a given altitude, thereby describing the design space and energy potential of AWES. As above, the data set is split by times of positive (left) and negative (right) SHF calculated in WRF. Times of unstable stratification show an almost constant distribution above 200 to 300 m. Stably stratified boundary layers show a steep increase of high wind speed ($U > 12$ m/s) probability up to about 500 m above which this value stays almost constant. A low chance of continuously increasing wind speed exists during times of very stable stratification leading to a wider spread of wind speeds aloft.
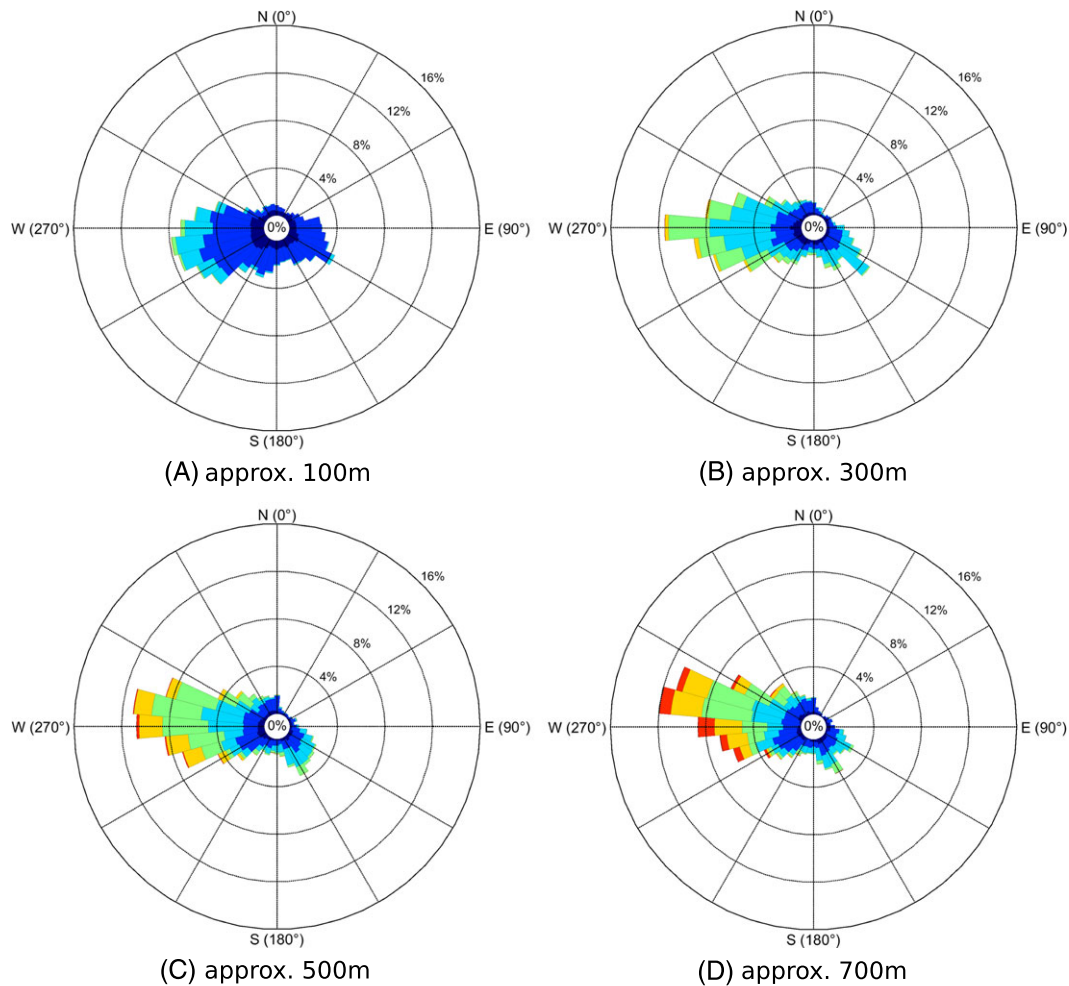
FIGURE 11 Wind direction and speed of the whole 6-month light detection and ranging measurement campaign between about 100 and 700 m represented as wind roses [Colour figure can be viewed at wileyonlinelibrary.com]

4.3 | Wind roses

Figure 11 depicts the wind roses at four different altitudes for the whole 6 months measurement campaign. The dominant wind direction is west, rotating from southwest to northwest with increasing altitude. An average rotation of about +30° between 100 and 1000 m as well as an increase in wind speed and a reduction in variability can be observed,[15] following the expedited trends in the northern hemisphere.[38]

4.4 | Turbulence intensity

Mid-altitude wind energy systems will benefit from relatively steady wind conditions with reduced turbulence fluctuation at higher altitudes. This reduction in variability reduces the energy intermittency and thereby improves the grid feed-in qualities of AWES. Variability in the wind velocity is quantified by the longitudinal, lateral, and upward TI. We focus on the longitudinal fluctuations along the direction of the 10-minute mean wind velocity. IEC standard 6[43] defines *TI* as the ratio between the 90% quantile standard deviation of the wind speed at a given height σ_U and the 10-minute mean wind speed *U*:

$$TI = \frac{\sigma_U}{U}. \tag{4}$$

Cup and sonic anemometers deliver high resolution measurements and can resolve high-frequency fluctuations at the scale of multiple *Hz*. While average wind speeds measured by LiDAR and other anemometers are generally in accordance with each other, TI values can differ due to different temporal and spatial resolution of the measurement technique.[44] The single beam DBS setup of the LiDAR, which produced the data we consider, requires the laser to adjust its orientation every 3 to 5 seconds. This relatively long sampling period results in a limited resolution and different standard deviation compared to other measurement techniques. Previous studies[45] have shown a correlation between LiDAR TI_{Lidar} and sonic turbulence measurements for lower altitudes. As of now, no high-altitude measurement device can reliably gather high-frequency data. Even though the LiDAR TI could not be independently validated, our results follow expected trends and can function as a long-term estimate of TI in higher altitudes.
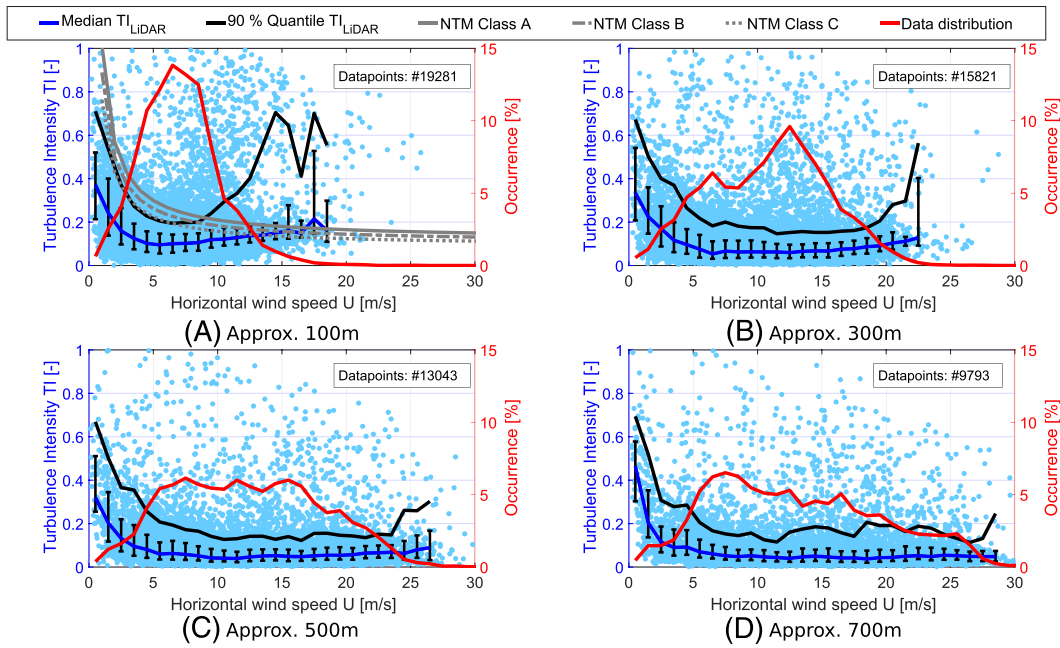
FIGURE 12 Comparison of light detection and ranging (LiDAR)-based turbulence intensity (TI_{LiDAR}) over horizontal wind speed U between 100 and 700 m during the six months measurement campaign. The black line visualizes the 90% quantile for comparison with the Normal Turbulence Model (NTM) turbulence classes defined by IEC standards 61400.[43] The median is represented by the blue line with error bars corresponding to P25 and P75. Data density is shown in red [Colour figure can be viewed at wileyonlinelibrary.com]

Figure 12 shows TI_{Lidar} as a function of mean horizontal wind speed for four different altitudes (measurements in light blue in the background) and the data density in red. The errorbars along the median (blue line) indicate the 25th and 75th percentile. Figure 12A includes the TI TI_{NTM} defined by the Normal Turbulence Model (NTM) in IEC standard 61400.[43]

$$TI_{NTM} = \frac{I_{ref}(0.75U + b)}{U} \qquad b = 5.6 \, m/s. \qquad (5)$$

Turbulence classes are defined by the 90% quantile of the turbulence standard deviation at hub height and approximated by $I_{refA} = 0.16$, $I_{refB} = 0.14$, or $I_{refC} = 0.12$. Measurements at a height of 100 m generally have good accordance with the C turbulence class, associated with the flat agricultural land surrounding the measurement location. The increase in TI_{LiDAR} for high wind speeds is likely caused by the small sample size and the wide scatter of these assessments. The fairly high amount of high TI_{LiDAR} outliers could be caused by the reduced data quality after the power outage.

The overall trend of average TI_{LiDAR} with altitude is shown in Figure 13. The data is split by WRF modeled SHF, with positive SHF indicated in red and negative SHF in blue, and the entire data are summarized in black. As expected, stable stratification (associated with negative SHF) experiences weaker turbulence than unstable stratification.[38] These trends remain almost constant above 500 m up to maximum measurement height. AWES will therefore have to withstand low but still existing turbulence induced fatigue loads. The error bars, which have been omitted for the entire data, set to maintain readability, along the median indicate the 25th and 75th percentile. The asymmetrical error bars during times of positive SHF indicate a tendency toward higher TI_{LiDAR} at all altitudes. Times of negative SHF show a low, almost symmetric TI_{LiDAR} distribution. The 90% quantile (black solid line) follows a similar trend, but increases slightly at very high altitudes possibly because of the limited availability aloft.

4.5 | Diurnal variability

The characterization of wind speed and turbulence diurnal variability is essential for AWES flight path optimization and sizing. We expect the diurnal cycle to be relatively weak because of the high cloud cover[46] during the measurement period at Pritzwalk (compare Figure 4). Figures 14 and 15 show the hourly average wind speed $\overline{U}$ and estimated TI $\overline{TI}_{LiDAR}$ variability as a function of altitude and time of day.[38] An almost constant average wind speed at 90 m suggests that this is approximately the reversal height, which is defined as the height of minimal variablility of the long-term wind speed.[23] Wind speeds below this altitude show lower wind speeds during night and higher wind speeds during day. Above the reversal height the wind speed increases during night because of a reduction in vertical turbulent momentum convergence because of the formation of near-surface stable stratification and is slowed down during day because of enhanced momentum transport because of buoyant generation of turbulence kinetic energy. Average wind speeds slowly increase at altitudes between 400 and 800 m over the course of the night, which peaks in the early morning, just before the convective boundary layer erodes this structure. Average wind speeds at these altitudes slow down in the late morning as the turbulent boundary layer reaches these altitudes. This is visualized by the increase in TI after sunrise. Around noon, average $\overline{TI}_{LiDAR}$ reaches its maximum at all altitudes, which coincides with an unstable stratification and results in low wind shear. Even
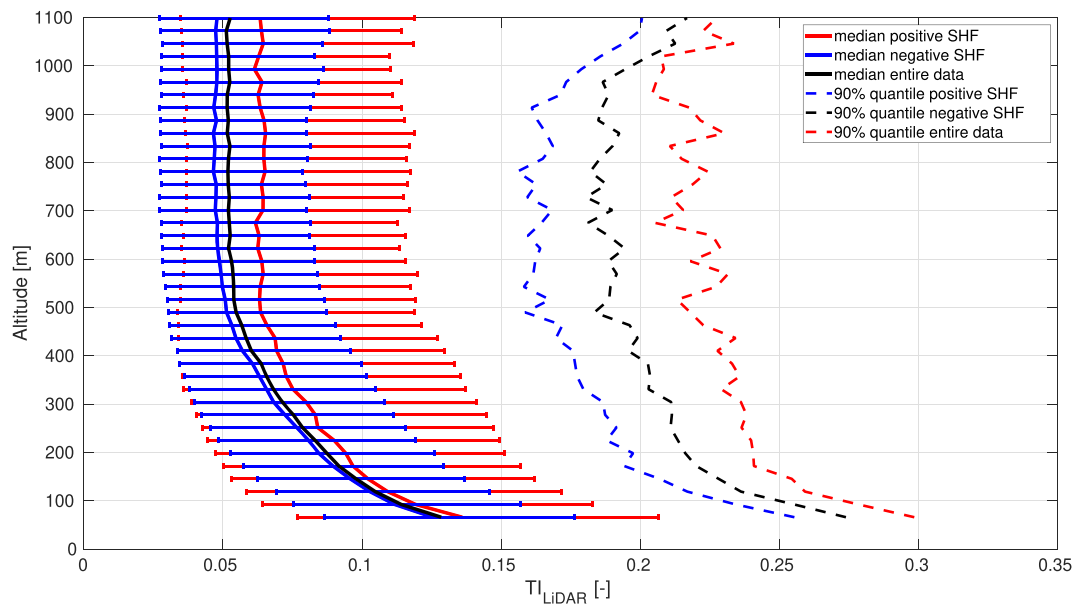
FIGURE 13 Turbulence intensity trend over altitude estimated based on 6-month light detection and ranging (LiDAR) measurements. The error bars visualize the median, P25 and P75 values for times of positive surface heat flux (SHF) (red) and negative SHF (blue). Error bars for the entire data set are not shown to maintain readability. The dashed lines show the 90% quantile as used by the IEC 61400 standards[43] [Colour figure can be viewed at wileyonlinelibrary.com]
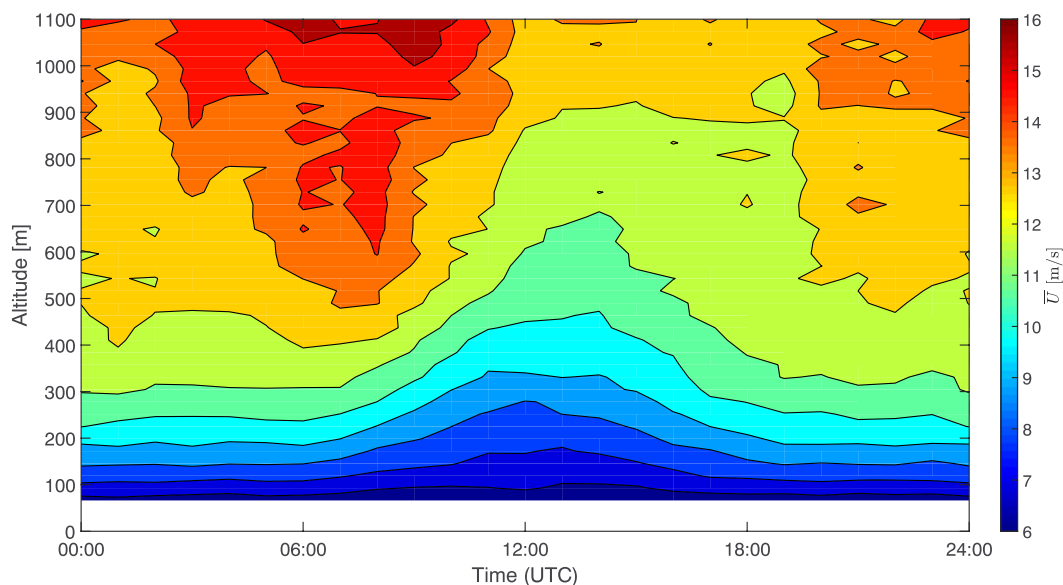

FIGURE 14 Six-month average diurnal variation of hourly mean wind speed $\overline{U}$ over altitude [Colour figure can be viewed at wileyonlinelibrary.com]

though $\overline{TI}_{LiDAR}$ increases almost simultaneously at all altitudes, wind speed changes are time delayed, probably caused by inertia of the air. These averaged values can not represent high-frequency fluctuations of constantly changing wind speed profiles but visualize typical diurnal changes. They further demonstrate that AWES benefit from adjusting their operating altitude to stay within a certain wind speed range or minimize tether drag and weight by flying as high as necessary and as low as possible.

4.6 | Representative wind conditions

Average wind conditions shown in previous subsections combine many different events. To improve physical insight and to illustrate the relationship between SHF and wind profile shape, an atypical and a more typical 24-hour period (see Figures 16 and 17) are analyzed in detail. The figures show the 10-minute mean horizontal wind speed contour in the top subfigure and the wind speed profile and direction in the bottom subfigure for 2 days in September 2015 from noon to noon. WRF-calculated SHF is plotted against the secondary axes on the right in the top subfigure. The white space represents missing or filtered data. Wind directions are defined according to section 2 by a positive clockwise rotation with 0° coming from north. The black X in each profile marks the altitude of highest wind speed and ○ the optimal operating altitude according
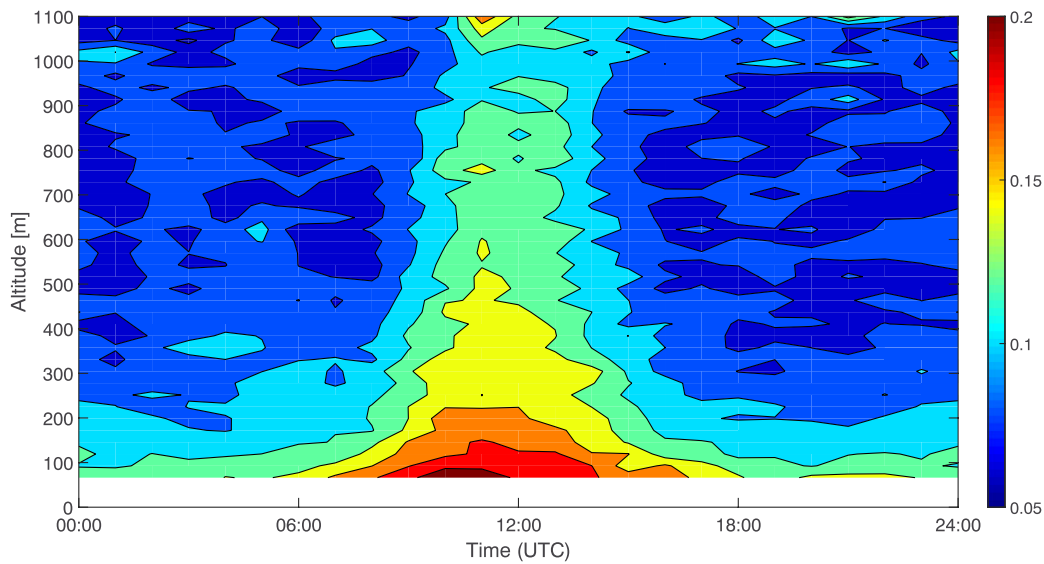
FIGURE 15 Six-month average diurnal variation of hourly mean turbulence intensity $\overline{TI}_{LiDAR}$ [Colour figure can be viewed at wileyonlinelibrary.com]
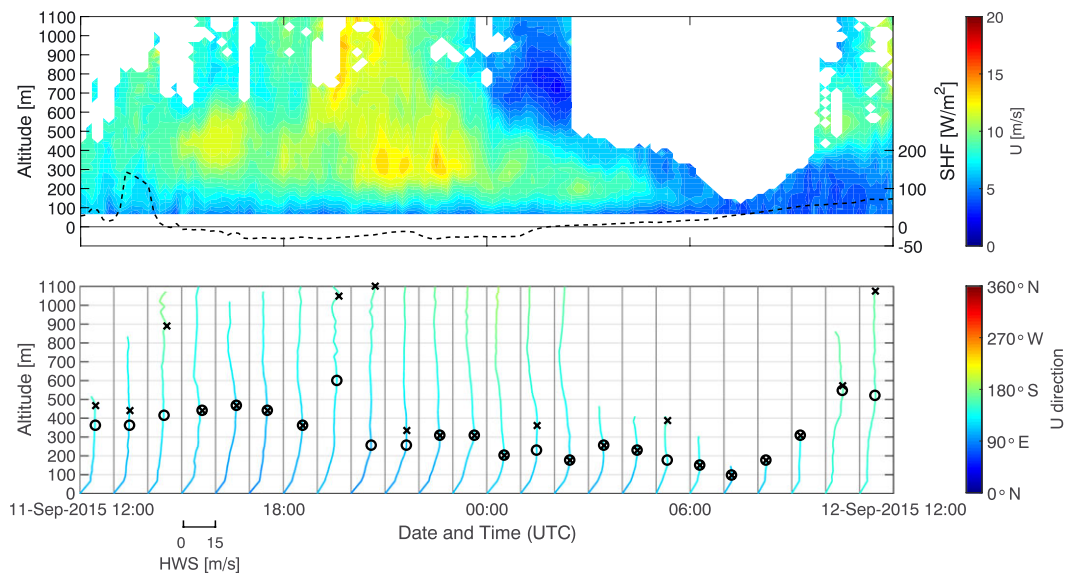

FIGURE 16 Visualization of measured 10-minute mean wind speed, wind direction between September 11 and 12, 2015. The top figure shows the wind speed and Weather Research and Forecasting-calculated surface heat flux (SHF) (dashed line). The bottom figure shows each hours 10-minute mean wind speed profile colored according to wind direction. The X marks the altitude of highest wind speed and ○ the optimal operating altitude according to section 5 [Colour figure can be viewed at wileyonlinelibrary.com]

to section 5, which often do not coincide due to the misalignment losses associated with a higher elevation angle.[14] Figure 16 shows one of the days, which was previously investigated with regard to CNR (see Figure 5).

On September 12, the advection of warm air lead to the formation of low level clouds within the investigated area of northeastern Germany. The atmosphere could be characterized as unstable, because of the temperature difference of about 45 K between the surface and 500 hPa, which lead to thunderstorms and rain during the afternoon and evening, which mostly ceased by September 12. The wind speed profile in Figure 16 shows fairly strong mixing during the afternoon and night of September 11. In the morning of September 12, data availability is limited due to low altitude clouds (see Figure 5). After 9 AM, the availability increases again, accompanied by a reduction of cloud cover.[28,47,48] The altitude of highest observed wind speed stays fairly constant throughout the entire day and mostly remains within the lowest 500 m of the atmosphere. Optimal operating altitudes (see section 5) mostly coincides with highest wind speed. Misalignment losses will be fairly small due to the low elevation angle. In contrast to the average wind direction (qest; see Fgure 11), the prevalent wind direction for this day is east southeast, with relatively little change of direction with altitude.

By September 21, the low-pressure system, which was responsible for the changeable weather of previous days, mostly disappeared.[28,47,48] The following high-pressure zone and the accompanying rainfall on its border region over northeastern Germany quickly decayed. Cumulus cloud banks formed during the noon hours over northern Germany. In contrast to September 12, the data in Figure 17 shows a rather average
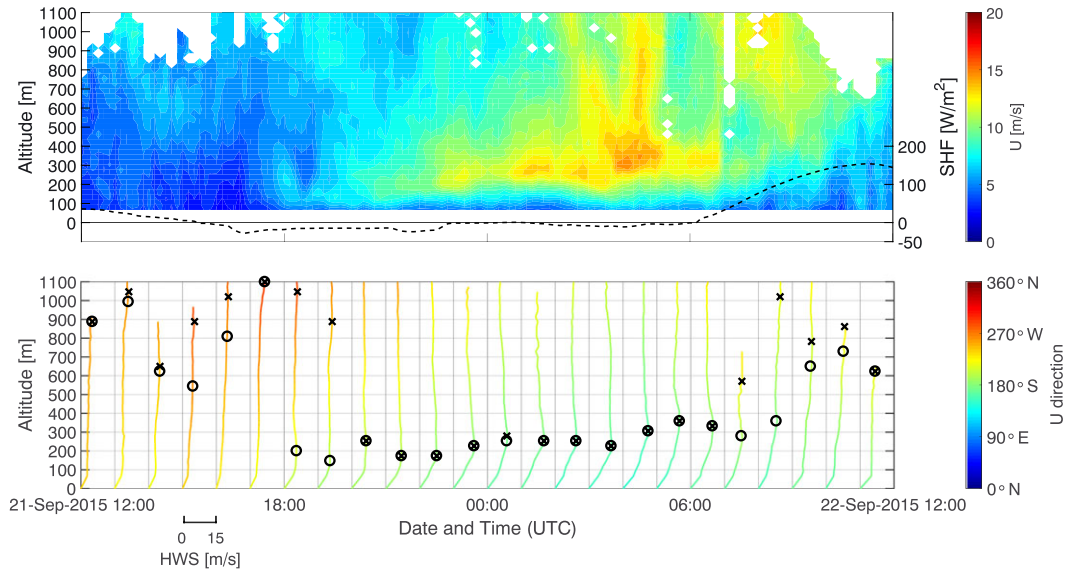
FIGURE 17   Visualization of measured 10-minute mean wind speed, wind direction between September 21 and 22, 2015. The top figure shows the wind speed and Weather Research and Forecasting-calculated surface heat flux (SHF) (dashed line). The bottom figure shows each hours 10-minute mean wind speed profile colored according to wind direction. The X marks the altitude of highest wind speed and ○ the optimal operating altitude according to section 5 [Colour figure can be viewed at wileyonlinelibrary.com]

day with a typical diurnal cycle and the development of a low level jet during the night. The daytime of September 21, 2015 shows an unstable stratification defined by strong mixing and high turbulence resulting in an almost uniform wind speed profile. The altitude of highest wind speed is in the higher parts of the boundary layer above 600 m. Even though overall wind speeds are fairly low, optimal operating altitudes are above 600, which leads to significant misalignment losses. After 18:00 UTC, the computed optimal altitude drops below 300 m because of low wind shear above. After sunset around 19:00 UTC, we observe the decoupling of the flows below and aloft caused by the development of a stable stratification, because of the reduction of vertical mixing.[23] The development of a low level jet is indicated by wind speeds of about 15 m/s between 200 and 400 m above ground, while wind speeds below and above are significantly slower. The optimal operating altitude coincides with the altitude of the low level jet. Furthermore, we observe a change in wind direction from southwest to southeast that approximately coincides with the formation of the low level jet, which is consistent with a stronger down-gradient flow near the surface. Sunrise at 7:00 UTC warms the surface and leads to the development of a mixing layer which over time increases in height.[15] The westwards wind direction throughout this day is more in line with the typical wind direction at Pritzwalk.

Relying on wind statistics or average diurnal variation is not sufficient when planning flight paths and operating AWES as a given day can differ significantly. Dynamically optimizing AWES trajectory and operating altitudes maximizes power production and mitigates dynamic loads. The disconnect between optimal operating altitude and altitude of the highest wind speed, which will be even more pronounced when losses such as tether drag and weight are taken into account, is clearly visible.

5 | POWER ESTIMATION

This section presents an analysis of the theoretical mechanical power and optimal altitude of an AWES based on measured wind speeds. The scope of this investigation is limited to the estimation of traction power using a ground generator (pumping mode) AWES. The model of a ground-generator system is adapted from Schmehl et al,[14] based on Loyd's approximation.[49] The estimated optimal power per unit lifting area of the wing p_{opt} is described by:

$$p_{opt} = \frac{\rho_{air}}{2} U^3 \sqrt{c_L^2 + c_D^2} \left[1 + \frac{c_L}{c_D}\right]^2 f_{opt} \left(\cos\theta \cos\phi - f_{opt}\right)^2. \tag{6}$$

Losses associated with misalignment of the wind direction and the aircraft position (azimuth angle ϕ, elevation angle θ) are included in the model. Additional losses caused by gravity and tether drag are neglected. The tether speed v_t is nondimensionalized in the form of the reeling factor ($f = \frac{v_t}{U}$). We consider quasi-steady state with the wing moving directly cross-wind with a zero azimuth angle ($\phi = 0$) relative to the wind direction. As a result, lift F_L and drag F_D are geometrically related to the radial ($v_{a,r} = (\cos\theta \cos\phi - f)v_w$) and tangential ($v_{a,t} = (\cos\theta \cos\phi - f)v_w \frac{F_L}{F_D}$) apparent velocity components. We assume optimal reeling speed ($f_{opt} = \frac{1}{3}\cos\theta \cos\phi$). The elevation angle is derived from altitude z and tether length L ($\theta = \arcsin(\frac{z}{L})$). Lift $c_L = 1.7$ and drag coefficient $c_D = 0.06$ are kept constant and assumed representative of an AWES. Air density ρ_{air} is calculated by a linear approximation of the standard atmosphere[50] ($\rho_{air}(z) = 1.225 kgm^{-3} - 0.00011 kgm^{-4} z$).

Figure 18 shows a heat map of the total probability distribution of optimal wind power and optimal flight altitude assuming a constant tether length of $L=1500$ m. The color scheme is cubic to account for the nonlinear relationship between wind speed and power. The continuous white line shows the probability distribution of optimal altitude over the whole p_{opt} range and is associated with the top abscissa. The dashed white line shows the probability distribution of optimal power over the whole altitude range and is associated with the right hand ordinate axis. Optimal traction power for the given system has the highest frequency below $p_{opt} < 1000 kW/m^2$ because of high chance of low wind speeds and low wind shear (see Table 1). Even at higher altitudes, the most probable traction power is below this value as wind speeds are still fairly low but increase enough that higher losses due to misalignment (θ in Equation 6) are offset. Altitudes between 200 and 700 m show higher but less frequent optimal power production because of higher wind shears and low level jets. Whether AWES will be able to harvest these winds or will be designed to avoid them because of increased mechanical loads remains to be seen. The most likely operating altitudes, based on measured wind conditions, are between 150 and 400 m, peaking at 300 m. However, the possibility for AWES to operate at altitudes above 700 m enables them to increase overall capacity.
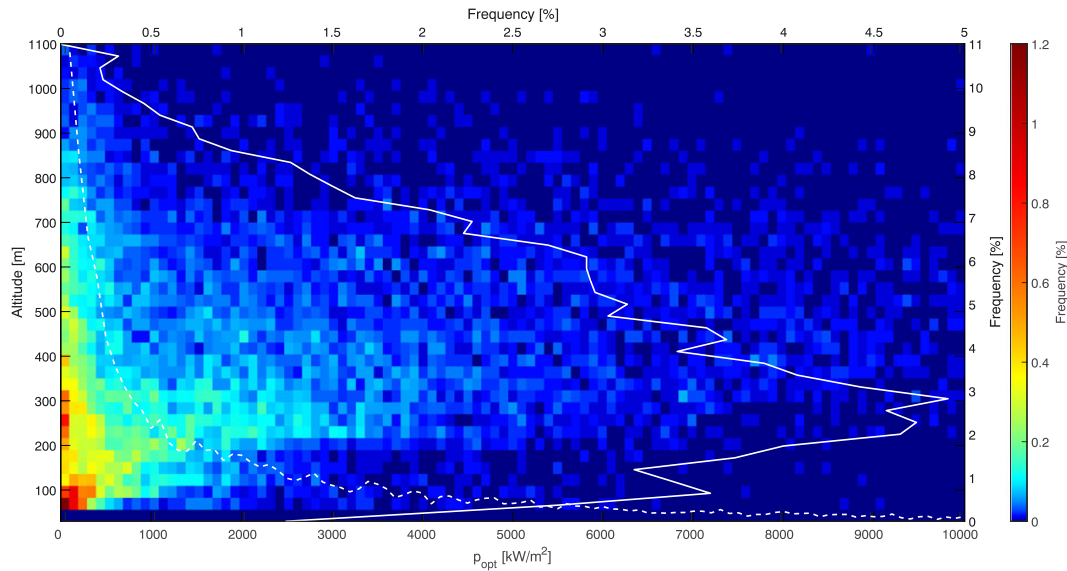

FIGURE 18 Probability of optimal traction power over optimal operating altitude. The continuous white line shows the frequency of optimal operating altitude for the entire power range (top abscissa axis) and the dashed white line shows frequency of optimal traction power for the whole altitude range (right ordinate axis) [Colour figure can be viewed at wileyonlinelibrary.com]
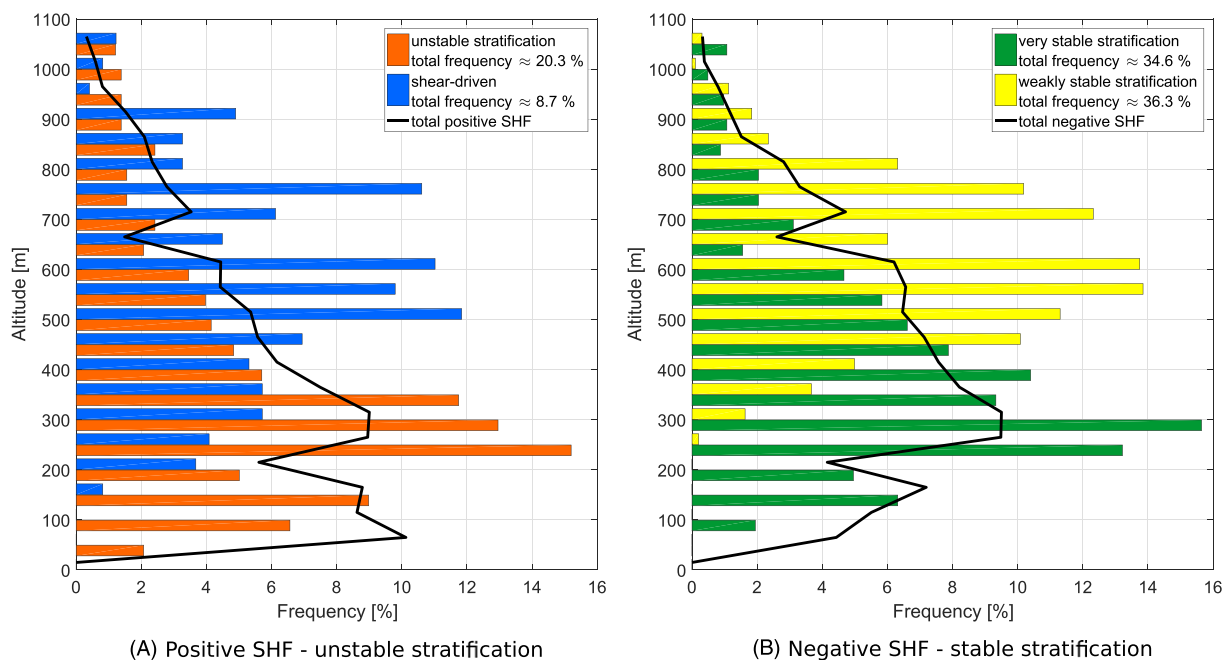

(A) Positive SHF - unstable stratification   (B) Negative SHF - stable stratification

FIGURE 19 Probability distribution of surface heat flux (SHF)-clustered optimal operating altitude for times of positive SHF A, and negative SHF B, (black lines) as well as the two respective substates (see Table 1) [Colour figure can be viewed at wileyonlinelibrary.com]

Splitting the data by heat flux reveals the impact of stratification on optimal flight altitude and power. Figure 19 shows the probability distribution of optimal operating altitude for times of positive SHF (A) and times of negative SFH (B) as defined in section 4.1. The bars represent the K-means clustered substates (see Figure 9). The black lines show the total probability for times of positive or negative SHF. Overall, flying above 500 m is rarely necessary to optimize power production. Only times of shear driven and weakly stable stratification benefit from operating above 500 m because of the stronger wind shear up to altitudes above 600 m. During times of unstable stratification, optimal operating altitude is between 300 and 400 m because of lower wind speeds and low wind shears above this altitude. Times of very stable stratification often experience low level jets, which lead to a peak in wind speed between 200 and 400 m. Traction power between these substates varies significantly due to vastly different wind speeds, even though operating altitudes are comparable.

Figure 20 shows the optimal power p_{opt} (associated with the top abscissa axis) per unit wing area for a given tether length (L = 500 - 2500m). Each subfigure uses a different range due to the disparity of p_{opt} in each substate. Wind speed profiles (blue line) are associated with the bottom abscissa axis and represent the average SHF-clustered wind speed. Subfigures are arrange as in Figure 9 with the top row representing times of
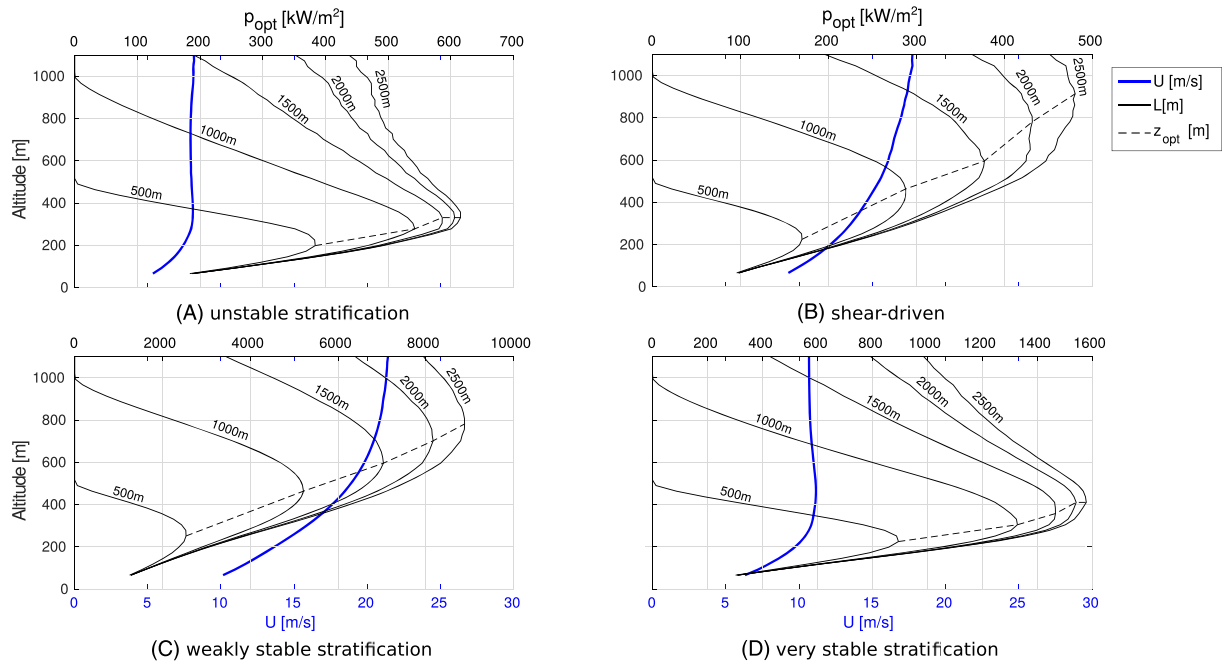

FIGURE 20 Optimal power[14] per wing area p_{opt} (black) and optimal operational altitude (dashed line) estimated based on mean K-means-clustered surface heat flux-sampled wind speed profiles (see Table 1—blue line) for varying tether length (L = 500 - 2500 m): A, unstable stratification, B, shear-driven stratification, C, weakly stable stratification, D, very stable stratification [Colour figure can be viewed at wileyonlinelibrary.com]
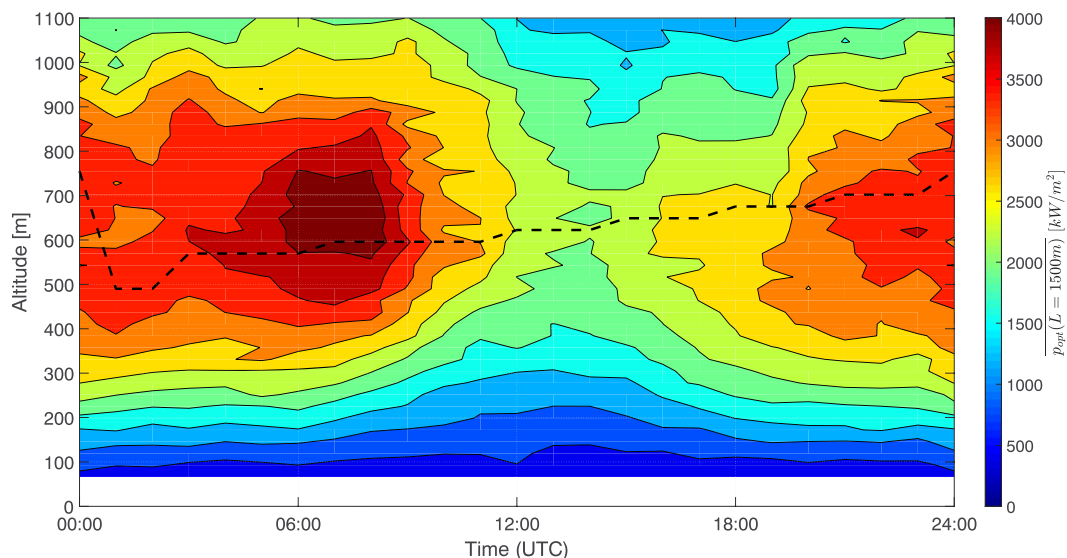

FIGURE 21 Diurnal variation of hourly mean traction power $\bar{p}_{opt}$ and optimal operating altitude (dashed line) assuming constant tether length of L = 1500 m and constant aerodynamic coefficients (c_L = 1.7 and c_D = 0.06) [Colour figure can be viewed at wileyonlinelibrary.com]

positive SHF and the bottom row are times of negative SHF. The dashed line connects the tetherŰlength-dependent optimal operating altitude z_{opt}. Times of unstable stratification (A) and very stable stratification (D) have an almost constant average wind speed profile above a certain altitude, which is why optimal power production peaks at these heights. Furthermore, an increase in tether length leads to diminishing returns as the misalignment losses are proportional to $\cos\theta$. Times of shear-driven stratification (B) and weakly stable stratification (C) benefit from longer tethers and higher operating altitudes. The higher overall wind speeds during these times lead to far higher traction power. However, actual operating altitude will likely be lower as the model neglects tether weight and drag, which are proportional to tether length.

Figure 21 shows the diurnal cycle of hourly averaged traction power per unit lifting area for constant $L = 1500$, $c_L = 1.7$ and drag coefficient $c_D = 0.06$ to estimate diurnal AWES power variation. The dashed line illustrates the optimal operating altitude which remains between 500 and 700 m through out most of the day. These altitudes are above the previously described, SHF-sampled values (see Figure 20) and mostly above the corresponding height during the representative days (see Figures 16 and 17). This difference is due to the fact that stratification is not only dependent on time of day but also affected by large-scale weather and climate phenomena. Traction power is highest during the night as average wind speeds and wind shears are higher. Average traction power decreases by almost 50% around noon as these times are more likely to be associated with unstable stratification, low wind shear and speed. While hourly average wind data might give a good long-term estimate, it can not represent the vastly different wind conditions that AWES will need to adapt to in order to optimize power production. This effect will be amplified when considering additional tether losses. Therefore, high-resolution wind data are needed to optimize power production and control the flight path during operation.

6 | CONCLUSION AND OUTLOOK

We have presented an evaluation of high resolution mid-altitude wind speed measurements from a 6-month measurement campaign in Pritzwalk, northern Germany. The onshore measurement location surrounded by flat, open, agricultural land was chosen due to its presumed suitability for the deployment of AWES. Based on the pulsed wind LiDAR data gathered up to an altitude of 1100 m, we have produced a statistical characterization of the prevailing wind conditions as well as an estimate of ideal power production and optimal operating altitude for the chosen location and time period. The results characterize important meteorological effects such as the influence of stratification on vertical wind speed profiles, wind direction, and TI (including mean diurnal cycles), which need to be considered for any mid-altitude wind energy device that aims to operate at comparable altitudes over flat terrain. We resolved multimodal wind speed statistics. The high vertical resolution enables the determination of optimal operating altitudes depending on AWES design.

We defined filters based on horizontal wind speed and CNR thresholds to increase the data availability while filtering out low-quality data. As a result , data availability at the lowest altitude (66 m) was about 85% and dropped steadily to about 25% at 1000 m. Cloud cover or fog affects data availability as most of the laser is absorbed or reflected leading to a high CNR within the cloud and very low backscatter above. Since CNR is related to aerosol content, it can be used as an indicator of mixing layer height. Determining a direct correlation between cloud cover and data availability is difficult and would require additional measurements such as aerosol concentration gathered by a ceilometer, since cloud cover does not give information on cloud height.

Wind statistics are affected by diurnal variability which leads to an increase of data availability around and after noon. By making use of a mesoscale reference simulation, we could show conditional sampling of our measurements which can be explained by increased thermal-mixing causing an increase in vertical aerosol transportation. Statistically different wind conditions were identified based on SHF data from the mesoscale model. Given the substantial effect of stratification on wind profiles, measuring the SHF or temperature at two near-surface altitudes along with winds would improve the classification of the wind conditions and reduce the error introduced by the difference between measurement and simulation. Using K-means clustering additional populations within stable and unstable stratification were identified. The superposition of these substates leads to a multimodal wind speed probability distribution. This multimodality is not accurately approximated with a two-parameter Weibull fit. A large reduction in error between measured data and fitted probability distribution between 100 and 500 m was achieved by superimposing two Weibull distributions of times associated with positive and negative SHF. The cumulative probability distribution of both states helps to estimate the altitude dependent energy potential of AWES.

Average diurnal variation impacts wind speed and TI. Vertical mixing and TI increases during daytime, because of positive SHF. Therefore, average wind speeds are lower, and wind shear is lower during day than during night.

Through the investigation of wind shear profiles during specifically chosen 24-hour windows, we infer various atmospheric stability and forcing conditions. We showed that strong thermal mixing, which occurs after sunrise of a typical diurnal cycle, leads to the time delayed onset of wind speed reduction with altitude. As a result, wind speed remains almost constant with altitude during periods of unstable stratification, reducing the necessary altitude of optimal energy production. Significant wind shear as well as the development of low level jets at an altitude between about 300 to 800˜m during stable conditions were observed. However, many days do not show these more typical diurnal variations and are affected by other large-scale weather phenomena.

Using an idealized traction power model that neglects gravity and tether drag, we determined the optimal operating altitude as well as an upper bound of traction power. Ideal altitudes for times of unstable and very stable stratification are between 300 and 500 m. During times of weakly stable stratification, AWES will benefit from flying between 500 and 800 m. Even though the average optimal altitude is around

350 m, AWES need to dynamically adapt their altitude to optimize power production. To do so, they will need high temporal and vertical resolution measurements. A more detailed model, including tether drag and weight, will yield lower optimal operating altitudes as those losses are proportional to tether length. Additionally, an investigation of the entire flight maneuver is necessary to estimate energy yield.

The 90% quantile of TI estimated based on standard deviation and mean LiDAR measured wind speed at 100 m shows comparable results to NTM turbulence classes defined by the IEC standard 61400. Up to an altitude of about 400 to 600 m the TI decreases, above which it remains almost constant. Since no independent, long-term, high-altitude wind turbulence measurements are available, these measurements give a good first estimation of average wind speed fluctuations, which helps to assess fatigue loads and lifetime of AWES. The benefits of operating at higher altitudes and the associated reduction of TI, need to be investigated and weigh against additional losses.

As expected for a northern hemisphere location, our measurements show an average clockwise wind rotation of about 30° . This directional change needs to be considered when optimizing the flight path of AWES and estimating the instantaneous power production.

In a subsequent analysis, we will compare these measurements to simulations from mesoscale WRF model used to produce the SHF time series used in this study. In particular, we will investigate the effect of implementing measurements via observation nudging. Comparing these results to the here discussed LiDAR measurements will deepen the understanding of mid-altitude winds and weather conditions. These simulations can supplement the annual statistics and give information about times that were not measured or where filtered out.

Finally, to further our understanding of mid-altitude winds and estimate the dynamic loads they cause, we will analyze results from LES using the Parallelized Large-eddy Simulation Model (PALM) developed by the Leibniz Universität Hanover, Germany. These simulations were driven by large-scale forcing generated from WRF. The resulting data set covers a wide spectrum of wind speeds and can be used to preliminary optimize the flight path as well as estimate mechanical loads and power of AWES.

ACKNOWLEDGEMENTS AND FUNDING SOURCES

CONFLICT OF INTEREST

We declare that neither the author nor any coauthor can identify any conflict of interest regarding the subject matter or materials discussed in this manuscript.

ORCID

Markus Sommerfeld 🅘 https://orcid.org/0000-0003-1116-5858

REFERENCES

1. Lunney E, Ban M, Duic N, Foley A. A state-of-the-art review and feasibility analysis of high altitude wind power in northern ireland. *Renew Sust Energ Rev*. 2017;68:899-911.

2. Fagiano L, Milanese M. Airborne Wind Energy: An Overview. In: 2012 American Control Conference (ACC). IEEE; 2012; Montreal, QC, Canada:3132-3143.

3. Cherubini A, Papini A, Vertechy R, Fontana M. Airborne wind energy systems: a review of the technologies. *Renew Sust Energ Rev*. 2015;51:1461-1476.

4. Gallice A, Wienhold FG, Hoyle CR, Immler F, Peter T. Modeling the ascent of sounding balloons: derivation of the vertical air motion. *Atmos Meas Tech*. 2011;4(10):2235-2253.

5. Archer CL, Caldeira K. Global assessment of high-altitude wind power. *Energies*. 2009;2(2):307-319.

6. Uwe F, Vlugt R, Schreuder E, Schmehl R. Dynamic model of a pumping kite power system. *Renew Energy*. 2015;83:705-716.

7. Optis M, Monahan A, Bosveld FC. Limitations and breakdown of monin-obukhov similarity theory for wind profile extrapolation under stable stratification. *Wind Energy*. 2016;19(6):1053-1072.

8. Schmehl R, et al. *Airborne Wind Energy; Advances in Technology Development and Research*. New York, NY: Springer Berlin Heidelberg; 2018. https://www.springer.com/gp/book/9789811019463, https://doi.org/10.1007/978-981-10-1947-0

9. Peña A, Hasager CB, Lange J, et al. *Remote Sensing for Wind Energy*. Denmark: DTU Wind Energy; 2013.

10. Matthias V, Bösenberg J. Aerosol climatology for the planetary boundary layer derived from regular lidar measurements. *Atmos Res*. 2002;63(3):221-245.

11. Sun X, Holmes H, Osibanjo O, Sun Y, Ivey C. Evaluation of surface fluxes in the WRF model: case study for farmland in rolling terrain. *Atmosphere*. 2017;8(12):197.

12. Wilmot C-SM, Rappenglück B, Li X, Cuchiara G. MM5 v3.6.1 and WRF v3.5.1 model comparison of standard and surface energy variables in the development of the planetary boundary layer. *Geosci Model Dev*. 2014;7(6):2693-2707.

13. Draxl C, Hahmann AN, Pena A, Nissen JN, Giebel G. Validation of boundary-layer winds from wrf mesoscale forecasts with applications to wind energy forecasting. In: 9th Symposium on Boundary Layers and Turbulence; 2010; Keystone, CO (US).

14. Schmehl R, Noom M, Vlugt R. *Traction Power Generation with Tethered Wings*, Airborne wind energy. Berlin, Heidelberg: Springer Berlin Heidelberg; 2013;23-45.

15. Stull RB. *An Introduction to Boundary Layer Meteorology*, Atmospheric and Oceanographic Sciences Library: Springer Netherlands; 1988.

16. Peña A, Gryning S-E, Floors R. Lidar observations of marine boundary-layer winds and heights: a preliminary study. *Meteorologische Zeitschrift*. 2015;24(6):581-589.

17. Paulson CA. The mathematical representation of wind speed and temperature profiles in the unstable atmospheric surface layer. *J Appl Meteorol*. 1970;9(6):857-861.

18. Emeis S. *Wind Energy Meteorology*, Green Energy and Technology. Berlin, Heidelberg: Springer Berlin Heidelberg; 2013.

19. SgurrEnergy. Galion: The definitive wind lidar.

20. Wind energy generation systems - part 12-1: Power performance measurements of electricity producing wind turbines; 2015.

21. Krishnamurthy R, Choukulkar A, Calhoun R, Fine J, Oliver A, Barr KS. Coherent doppler lidar for wind farm characterization. *Wind Energy*. 2013;16(2):189-206.

22. Bilstein M, Emeis S. The Annual Variation of Vertical Profiles of Weibull Parameters and their Applicability or Wind Energy Potential Estimation; 2010.

23. Gryning S-E, Floors R, Peña A, Batchvarova E, Brümmer B. Weibull wind-speed distribution parameters derived from a combination of wind-lidar and tall-mast measurements over land, coastal and marine sites. *Bound-Lay Meteorol*. 2016;159(2):329-348.

24. Clive P, Gordon M. Galion toolbox tutorial. SgurrEnergy; 2013.

25. Peña A, Gryning S-E, Hahmann AN. Observations of the atmospheric boundary layer height under marine upstream flow conditions at a coastal site: COASTAL BOUNDARY LAYER HEIGHT. *J Geophys Res-Atmos*. 2013;118(4):1924-1940.

26. Clive P. Sgurr energy—arc scan wind measurements for power curve tests; 2016.

27. Beck H, Kühn M. Dynamic data filtering of long-range doppler lidar wind speed measurements. *Remote Sens*. 2017;9(6):561.

28. Deutscher wetterdienst website. https://www.dwd.de/DE/leistungen/_functions/Suche/Suche_Formular.html?nn=13790.Accessed: 2018-06-05.

29. Davoust S, Jehu A, Bouillet M, Bardon M, Vercherin B, Scholbrock A, Fleming P, Wright A. Assessment and Optimization of Lidar Measurement Availability for wind turbine control: preprint. In: National Renewable Energy Laboratory (NREL); 2014; Golden, CO.

30. Eresmaa N, Karppinen A, Joffre SM, Räsänen J, Talvitie H. Mixing height determination by ceilometer. *Atmos Chem Phys*. 2006;6(6):1485-1493.

31. Seibert P, Beyrich F, Gryning S-E, Joffre S, Rasmussen A, Tercier P. Review and intercomparison of operational methods for the determination of the mixing height. *Atmos Environ*. 2000;34(7):1001-1027.

32. Emeis S, Schäfer K. Remote sensing methods to investigate boundary-layer structures relevant to air pollution in cities. *Bound-Lay Meteorol*. 2006;121(2):377-385.

33. Emeis S, Schäfer K, Münkel C. Surface-based remote sensing of the mixing-layer height—a review. *Meteorologische Zeitschrift*. 2008;17(5):621-630.

34. Skamarock WC, Klemp JB. A time-split nonhydrostatic atmospheric model for weather research and forecasting applications. *J Comput Phys*. 2008;227(7):3465-3485.

35. Dee DP, Uppala SM, Simmons AJ. The era-interim reanalysis: configuration and performance of the data assimilation system. *Q J R Meteorol Soc*; 137(656):553-597.

36. Nakanishi M, Niino H. An improved Mellor - Yamada Level-3 Model: its numerical stability and application to a regional prediction of advection fog. *Bound-Layer Meteorol*. 2006;119(2):397-407.

37. Troen I, Lundtang Petersen E. *European Wind Atlas*. Roskilde, Denmark: Risø National Laboratory; 1989.

38. Pal AS. *Introduction to Micrometeorology*. Cambridge, MA: Academic Press; 2001.

39. Bilir L, İmir M, Devrim Y, Albostan A. Seasonal and yearly wind speed distribution and wind power density analysis based on Weibull distribution function. *Int J Hydrog Energy*. 2015;40(44):15301-15310.

40. Gryning S-E, Batchvarova E, Floors R, Peña A, Brümmer B, Hahmann AN, Mikkelsen T. Long-term profiles of wind and weibull distribution parameters up to 600 m in a rural coastal and an inland suburban area. *Bound-Lay Meteorol*. 2014;150(2):167-184.

41. Monahan AH, He Y, McFarlane N, Dai A. The probability distribution of land surface wind speeds. *J Climate*. 2011;24(15):3892-3909.

42. Monahan AH, Rees T, He Y, McFarlane N. Multiple regimes of wind, stratification, and turbulence in the stable boundary layer. *J Atmos Sci*. 2015;72(8):3178-3198.

43. International Electrotechnical Commission et al.. Iec 61400-1: Wind turbines part 1: design requirements. International Electrotechnical Commission; 2005.

44. Sathe A, Banta R, Pauscher L, Vogstad K, Schlipf D, Wylie S. *Estimating Turbulence Statistics and Parameters from Ground- and Nacelle-Based Lidar Measurements: Iea Wind Expert Report*. Denmark: DTU Wind Energy; 2015. Grant no: 0602-02486B.

45. Sathe A, Mann J, Gottschall J, Courtney MS. Can wind lidars measure turbulence? *J Atmos Oceanic Tech*. 2011;28(7):853-868.

46. He Y, Monahan AH, McFarlane NA. Diurnal variations of land surface wind speed probability distributions under clear-sky and low-cloud conditions: WIND SPEED PDF UNDER CLEAR AND CLOUD SKY. *Geophys Res Lett*. June 2013;40(12):3308-3314.

47. Wetterzentrale website. http://www.wetterzentrale.de/.Accessed: 2018-06-05.

48. Sklima website. http://www.sklima.de/wetterlagen.php.Accessed: 2018-06-05.

49. Loyd ML. Crosswind kite power (for large-scale wind power production). *J Energy*. 1980;4(3):106-111.

50. Champion KSW, Cole AE, Kantor AJ. Chapter 14 standard and reference atmospheres.

51. SgurrEnergy Galion Lidar; 2016.